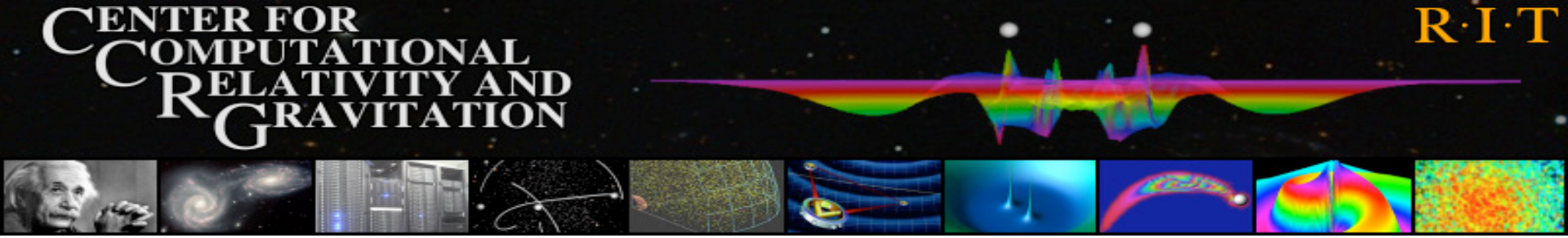

From binary black holes simulations to insights into astrophysics and gravitational waves

Carlos Lousto, Rochester Institute of Technology

Ecole Internationale Daniel Chalonge-Héctor deVega, Paris, January 21st, 2021

Overview

1. *Introduction*: NR Breakthrougths and first BBH orbital dynamics results: Hangup.

2. *Precessing dynamics*: Flip-flops, alignment instability, GW Beacons.

3. *Merger remnant:* Modeling of final mass and spin. Peak waveform amplitude and frequency. Applications to GW observations.

4. *Merger Recoils:* Generic and maximum astrophysical recoils. Applications to statistical distributions and 3C 186.

5. *NR Waveforms Catalogs:* Applications to GW observations, direct and complete binary parameter estimations.

6. GW190521: An extraordinary event.

7. Discussion: Getting ready for GW next detections: Highly spinning BBH, small mass ratios, BHNS. Pulsar Timing. LISA.

Extras:

- Extreme simulations: q=1/128, R/M=100, S/M^2=0.99, P/M=0.99, 3BHs & NBHs
- Numerical improvements: Extraction r$\rightarrow \infty$, 3PN-QC-ID,(α_0,β_0), h, CofM

1. Introduction

A Brief Historical Overview

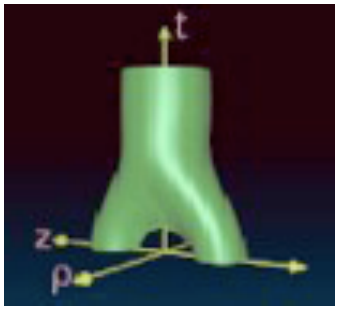

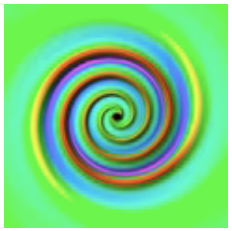

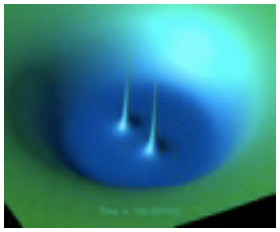

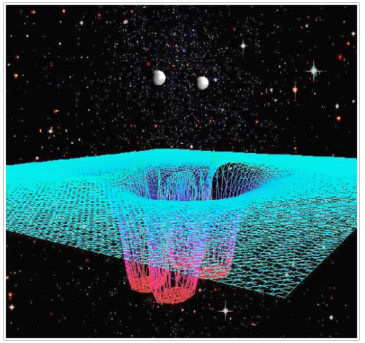

40+years of hard labor:

1964 First Simulation (Hahn & Lindquist)
Larry Smarr and Eppley in the '70
… then LIGO …
1990s Grand Challenge
BSSN-NOK evolution system
Puncture Initial Data (Brandt-Brügmann)
Gauge: Fixed Punctures (Alcubierre et al)
Lazarus (Campanelli et al)
2004 Corrotating Orbit (Brügmann et al)

Breakthrough:

2005 NR *Annus Mirabilis*
Binary Inspiral and Merger
Pretorius, PRL 95 (2005)
Moving Punctures (RIT & NASA)
Campanelli et al PRL 96 (2006)
Baker et al PRL 96, (2006)
(3 solutions in 4 months: July-Nov. 2005)

Numerical Relativity next:

2006+ GW Waveforms & Orbits,
Spin dynamics, Mass ratios,
GW Recoils, BH remnants,
BHs multiplets
2009+ Community Collaborations
2010+ Extreme BH Binaries
BH Binaries in a gaseous environment

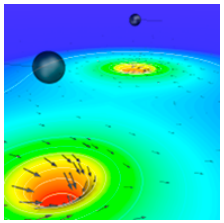

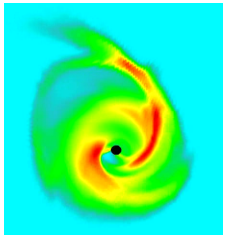

Spectral Einstein Code (SpEC):

Generalized Harmonic, but 1st order
Physical BCs
Highly-accurate, but less flexible (care needed to get BH-BH merger)
Extended to GRMHD (BH-NS)

Moving Puncture Codes:

LazEv: BSSN + Punctures, AMR, finite difference-accurate (8th order), but more flexible and robust (NBH - BH/NS/NS mergers)
Community Codes, including GRMHD (http://einsteintoolkit.org)

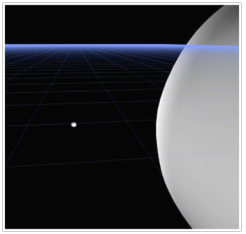

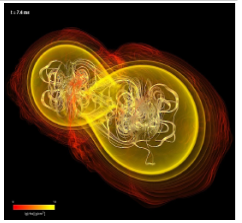

RIT vs. SXS techniques*

	LazEv	SpEC
Initial data		
Formulation of Einstein constraint equations	conformal method using Bowen-York solutions [37–39]	conformal thin sandwich [38, 40]
Singularity treatment	puncture data [41]	quasi-equilibrium black-hole excision [42–44]
Numerical method	pseudo-spectral [45]	pseudo-spectral [46]
Achieving low orbital eccentricity	post-Newtonian inspiral [47]	iterative eccentricity removal [48, 49]
Evolution		
Formulation of Einstein evolution equations	BSSNOK [50–52]	first-order generalized harmonic with constraint damping [11, 53–55]
Gauge conditions	evolved lapse and shift [56–58]	damped harmonic [59]
Singularity treatment	moving punctures [12, 13]	excision [60]
Outer boundary treatment	Sommerfeld	minimally-reflective, constraint-preserving [53, 61]
Discretization	high-order finite-differences [62, 63]	pseudo-spectral methods
Mesh refinement	adaptive mesh refinement [64]	domain decomposition with spectral adaptive mesh refinement [46, 59]

TABLE I. A comparison of the two independent numerical relativity codes described in the text. Each code uses different techniques to construct and evolve initial data for BBHs and to extract the emitted gravitational radiation. This table is based on Table I of Ref. [18].

From: G. Lovelace, C. Lousto et al. Class.Quant.Grav. 33 (2016) no.24, 244002

Total (and excellent) complementarity of both techniques!

Merger of Spinning Black Holes: Hang-Up Orbits

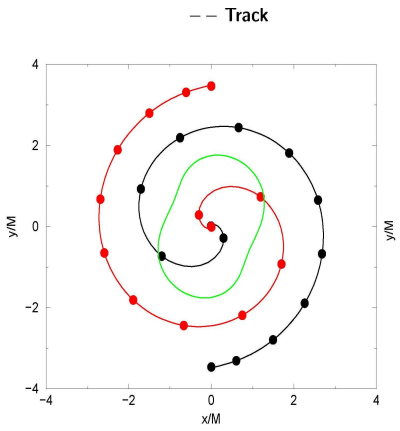

Figure 4: Puncture tracks for the $--$ configuration.

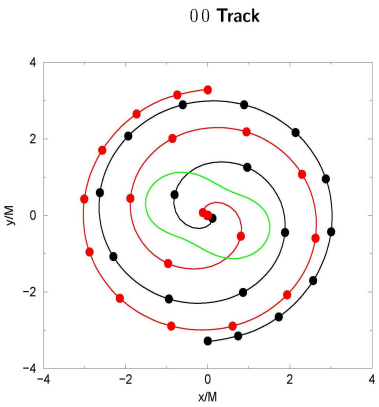

Figure 5: Puncture tracks for the 00 configuration.

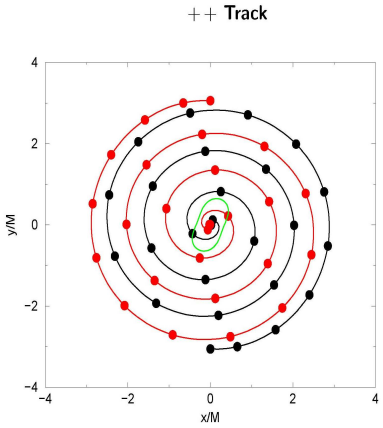

Figure 6: Puncture tracks for the $++$ configuration.

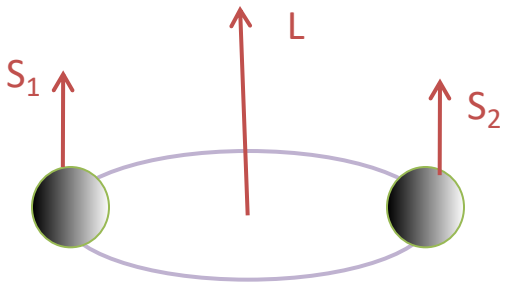

- Equal-mass BHBs
- $S_{1,2}/m^2 = \{-0.75, 0, 0.75\}$
- $M\Omega = 0.05$ (Starting "radius" the same).

- Hang-up effect due to strong repulsive spin-orbit interaction leaving behind a remnant with sub-maximal spin < 0.96) [Campanelli, Lousto, Zlochower, PRD 2006]: *cosmic censorship respected*!

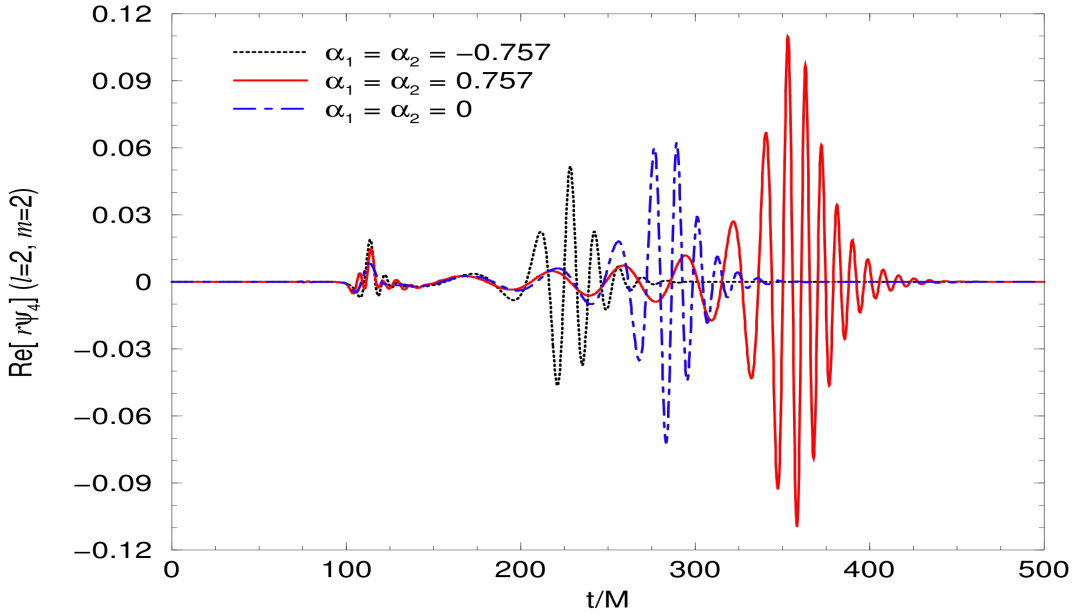

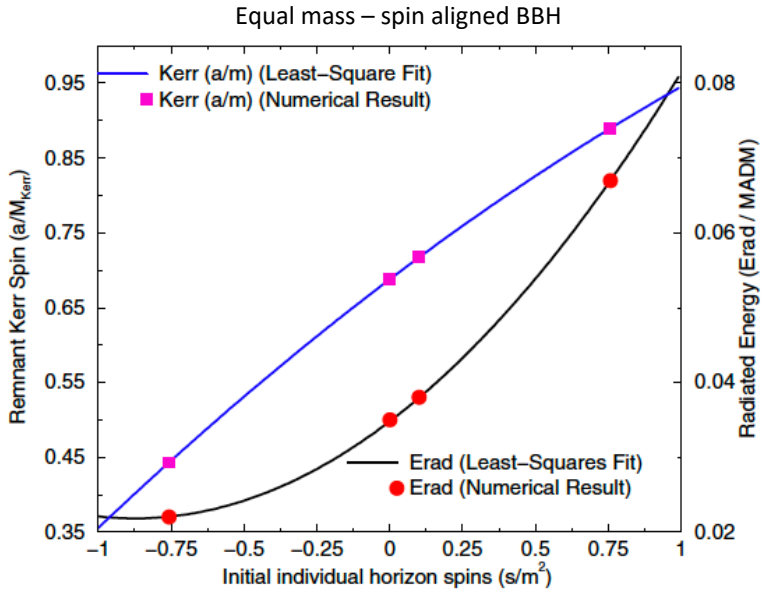

2. Precessing Spin Dynamics

Exploring BH Merger Spin Dynamics: Generic Binaries

- First merger of a generic, precessing BH binary [Campanelli, Lousto, Nakano and Zlochower, PRD 2009]

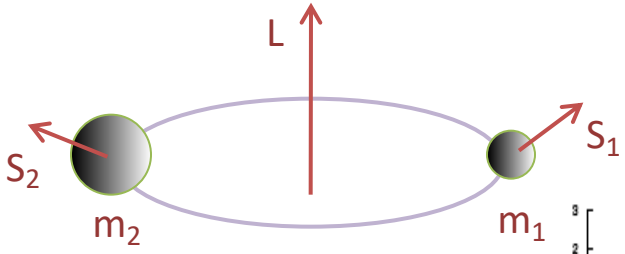

- Random Spin, non-equal mass, small eccentricity
  - $m_1/m_2 \sim 0.8$, $a_1/m_1 \sim 0.6$, $a_2/m_2 \sim 0.4$
  - spins initially at arbitrary orientations
  - complete 9 orbits prior merger
  - Comparison with 3.5PN inspiral for all l=2,3 modes.

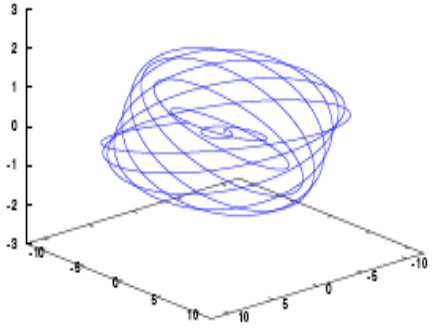

Trajectory difference $\underline{r} = \underline{x}_1 - \underline{x}_2$

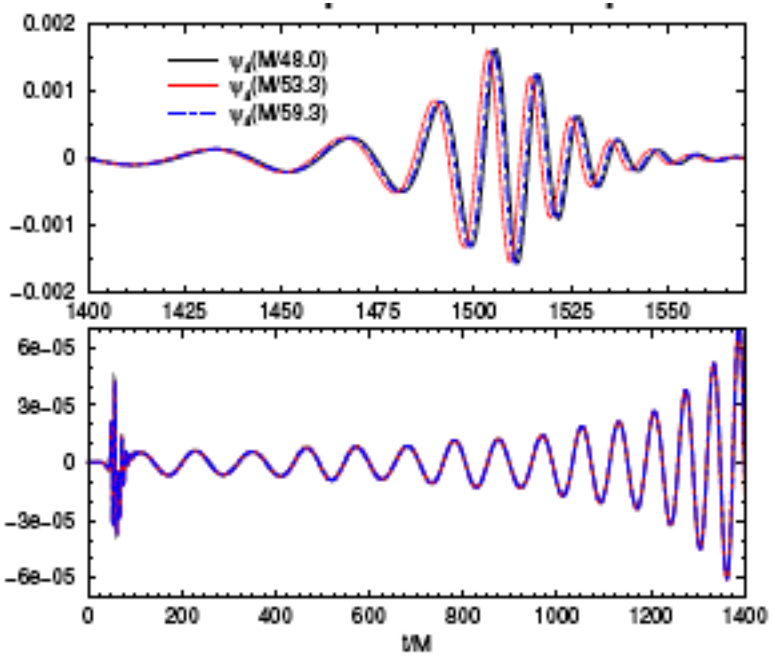

- These Simulations were Computationally Challenging!

"I have bet these numerical relativists that gravitational waves will be detected from black-hole collisions before their computations are sophisticated enough to simulate them. I expect to win,..."

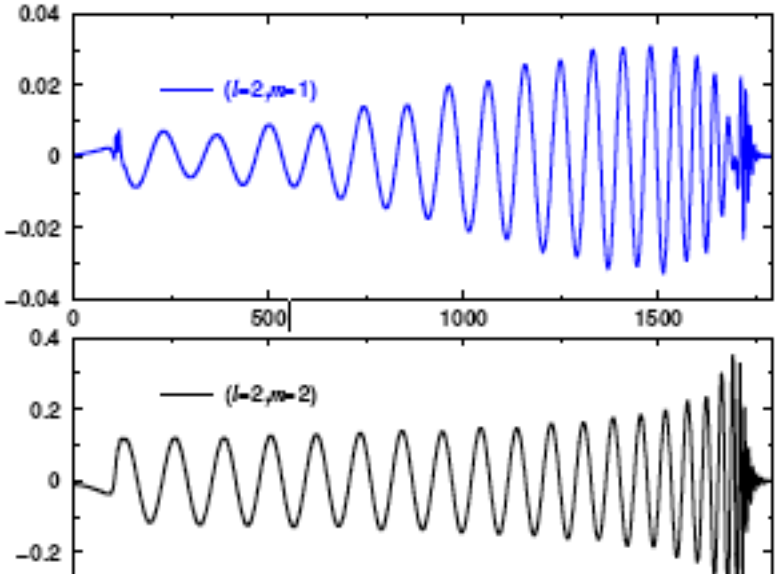

Compact binary mergers

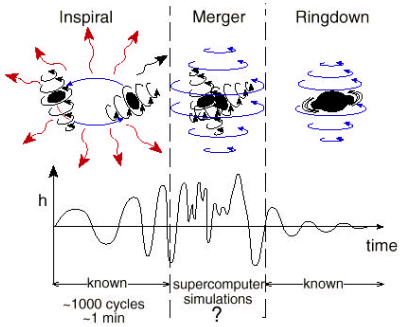

Reference: K.S. Thorne,
"Spacetime Warps and the Quantum World: Speculations About the Future,"
in R.H. Price, ed., *The Future of Spacetime* (W.W. Norton, New York, 2002).

Flip-flopping spins: A numerical simulation

Motivation: To further understand the dynamics of spinning (precessing) binary black holes

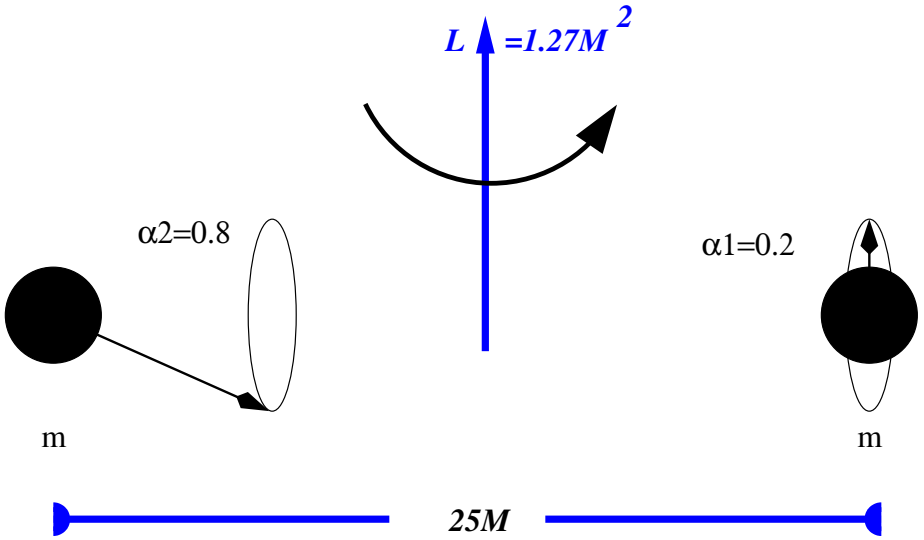

Equal mass binary with initial proper separation d=25M.
Unequal spins α_1=0.2 aligned with **L**
α_2=0.8 slightly misaligned with L such that **S**.**L**=0.

Run lasts for t=20,000M and makes 48.5 orbits before merger, 3 cycles of precession and one half of spin-flip.

After merger the final black hole acquires a recoil velocity of 1500 km/s.

Based on: C.O.Lousto & J.Healy, Physical Review Letters, **114**, 141101 (2015)

Flip-flopping spins: A visualization

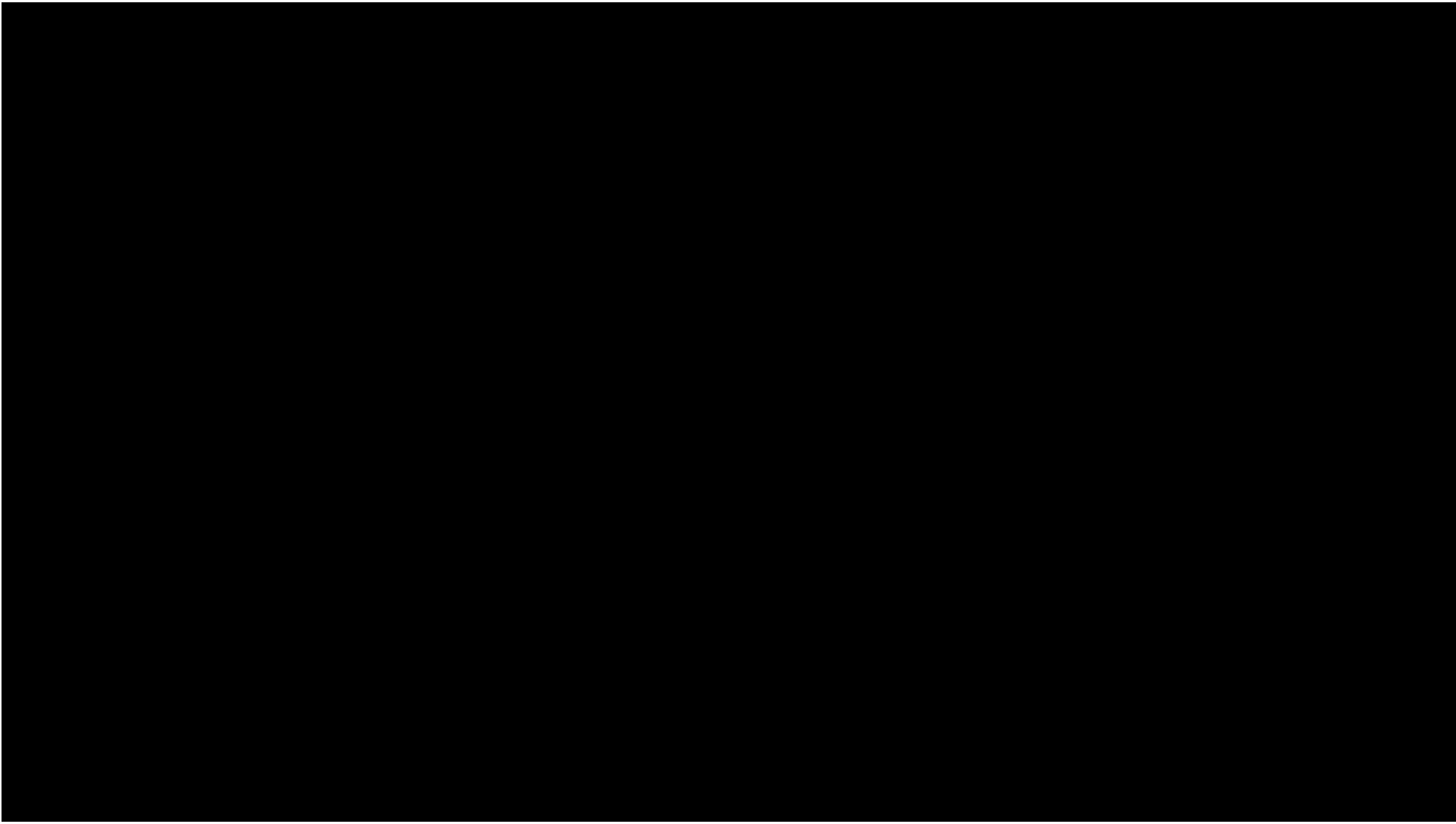

Unequal mass spinning binaries: 2PN analysis*

The flip-flopping frequency leading terms are now,

$$M\Omega_{1,2}^{ff} \approx \frac{3}{2}\frac{|1-q|}{(1+q)}\left(\frac{M}{r}\right)^{5/2} + 3\frac{S_1^L - S_2^L}{M^2}\left(\frac{M}{r}\right)^{3} sign(1-q)$$

The origin of the additional term for unequal masses scaling with $\sim r^{-5/2}$ is due to the non-conservation of the angle β between the two spins (as opposed to its conservation in the $q = 1$ case). These oscillations in β are due to the differential precessional angular velocity of $\vec{S}_1$ and $\vec{S}_2$ for $q \neq 1$ and hence provides the (precessional) scaling $r^{-5/2}$.

The maximum flip-flop angle is now,

$$1 - \cos(\Delta\theta_{1L}^{ff}) \approx \frac{2\alpha_2^2}{(1-q)^2}\left(\frac{M}{r}\right) + \frac{4\alpha_1\alpha_2^2 q}{(1-q)^3}\left(\frac{M}{r}\right)^{3/2}$$

From: C.O.Lousto, J.Healy & H. Nakano, Physical Review, **D93**, 044031 (2016)

Discussion: Observational effects

The leading flip-flop period is now given by

$$T_{ff} \approx 2,000\, yr\, \frac{(1+q)}{(1-q)} \left(\frac{r}{1000M}\right)^{5/2} \left(\frac{M}{10^8 M_\odot}\right).$$

which is much shorter than the gravitational radiation

$$T_{GW} \approx 1.22\, 10^6\, yr \left(\frac{r}{1000M}\right)^{4} \left(\frac{M}{10^8 M_\odot}\right),$$

alignment processes can be less effective than expected when the flip-flop of spins is taken into account.

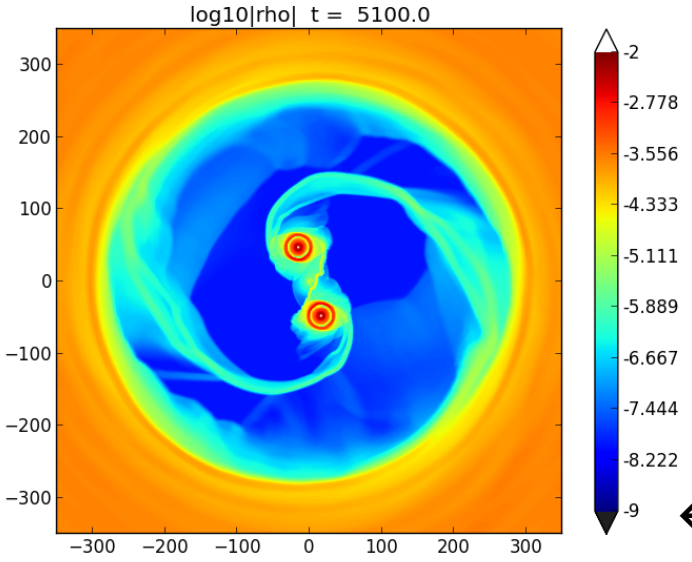

← Simulation by RIT group

Accretion disk internal rim will change location with spin orientation. This changes

- Efficiency of the EM radiation
- Spectrum of EM radiation (hard part)
- Cutting frequency of oscillations

Proper modeling using GRMHD simulations

X-shaped galaxies should show 'orange peeling' jets when they were about to merge

- For our simulation this corresponds to 1.2 seconds for 10Msun and 142 days for 10^8Msun

- The effect is still present in unequal mass binaries, (and BH-NS and NS-NS) with smaller flip-flop angles.

We need full numerical GRMHD simulations

Flip-flop instability*

2 PN Analytic study

$$d^2(\vec{S}_i \cdot \hat{L})/dt^2 = -\Omega_{ff}^2 \, \vec{S}_i \cdot \hat{L} + \cdots$$

$$\Omega_{ff}^2 = \frac{9}{4}\frac{(1-q)^2 M^3}{(1+q)^2 r^5} + 9\frac{(1-q)(S_{1\hat{L}} - S_{2\hat{L}})M^{3/2}}{(1+q)r^{11/2}} - \frac{9}{4}\frac{(1-q)(3+5q)\,S_{1\hat{L}}{}^2}{q^2 r^6} + \frac{9}{2}\frac{(1-q)^2 S_{1\hat{L}} S_{2\hat{L}}}{q r^6} + \frac{9}{4}\frac{(1-q)(5+3q)\,S_{2\hat{L}}{}^2}{r^6} + \frac{9}{4}\frac{S_0^2}{r^6} + 9\frac{(1-q)^2 M^4}{(1+q)^2 r^6}, \quad (1)$$

where $\vec{S}_0/M^2 = (1+q)\left[\vec{S}_1/q + \vec{S}_2\right]$.

$$\Omega_{ff}(q, \vec{\alpha}_1, \vec{\alpha}_2, R_c) = 0. \quad (2)$$

The solution of this quadratic equation for antialigned spins leads to two roots $R_c^{\pm}$.

$$R_c^{\pm} = 2M\frac{A \pm 2(\alpha_{2L} - q^2\alpha_{1L})\sqrt{B}}{(1-q^2)^2}, \quad (3)$$

$$A = (1+q^2)(\alpha_{2L}^2 + q^2\alpha_{1L}^2), \\ -2q(1+4q+q^2)\alpha_{1L}\alpha_{2L} - 2(1-q^2)^2$$

$$B = 2(1+q)\left[(1-q)q^2\alpha_{1L}^2 - (1-q)\alpha_{2L}^2 \right. \\ \left. -2q(1+q)\alpha_{1L}\alpha_{2L} - 2(1-q)^2(1+q)\right].$$

q>0.45

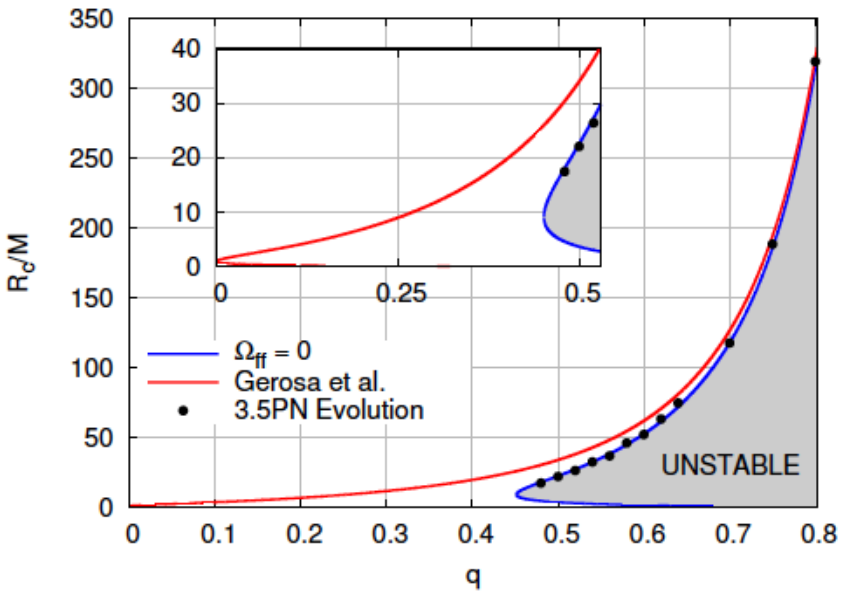

FIG. 3. The instability region, between $R_c^{\pm}$, as a function of the mass ratio, q, as the binary transitions from real to imaginary flip-flop frequencies (blue curve) for maximal spins $\alpha_{1L} = -1$ and $\alpha_{2L} = +1$. For comparison also plotted are $r_{ud\pm}$ from [8] (red curve). The dots correspond to 3.5PN evolutions.

From: C.O.Lousto & J.Healy, Phys. Rev., **D93**, 124074 (2016)

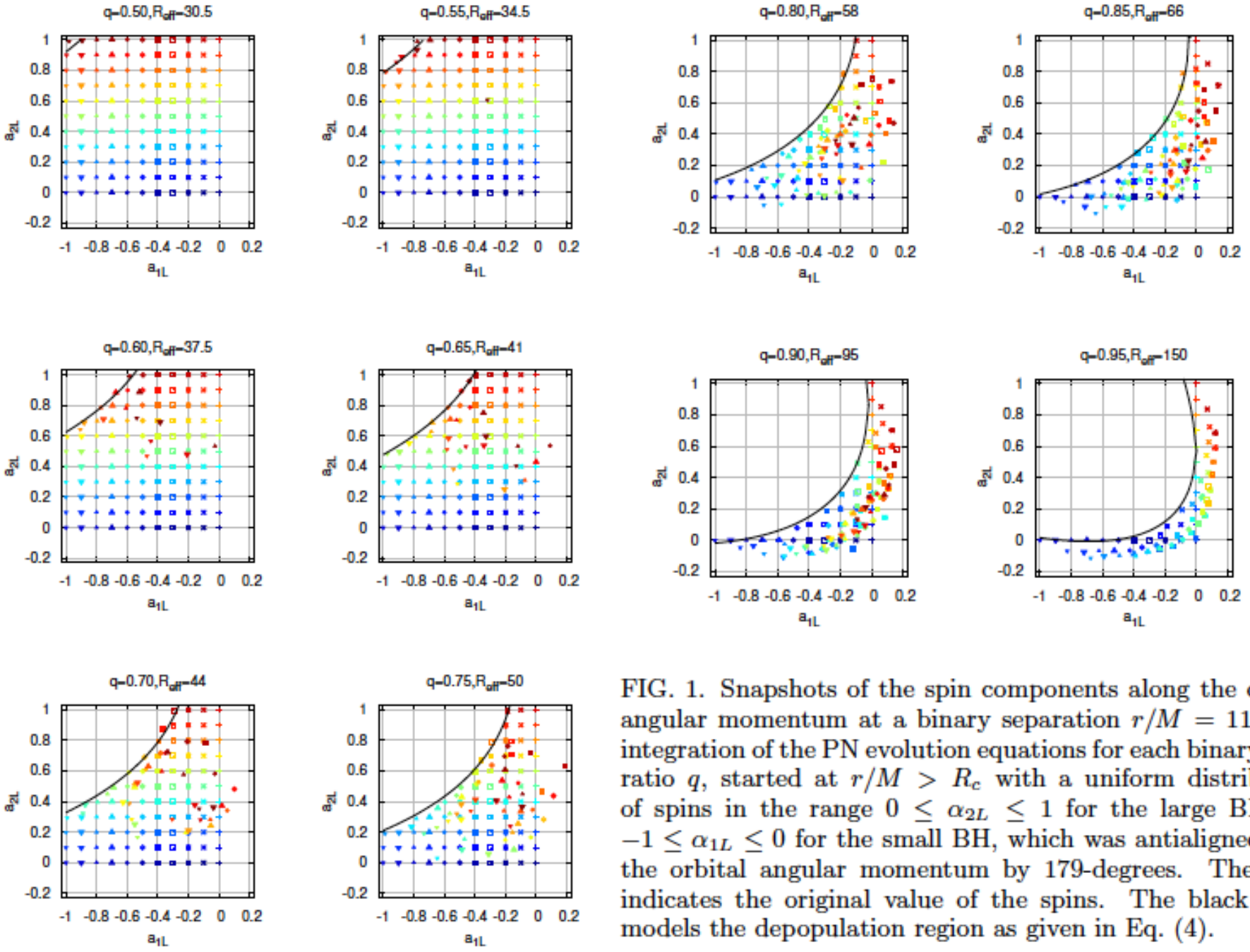

FIG. 1. Snapshots of the spin components along the orbital angular momentum at a binary separation $r/M = 11$. The integration of the PN evolution equations for each binary mass ratio q, started at $r/M > R_c$ with a uniform distribution of spins in the range $0 \leq \alpha_{2L} \leq 1$ for the large BH and $-1 \leq \alpha_{1L} \leq 0$ for the small BH, which was antialigned with the orbital angular momentum by 179-degrees. The color indicates the original value of the spins. The black curve models the depopulation region as given in Eq. (4).

References: Flip-flops and alignment instability*

Flip-Flopping Black Holes: Study of polar oscillations of BH spins

C. O. Lousto and J. Healy, Phys. Rev. Lett. **114**, 141101 (2015), arXiv:1410.3830 [gr-qc].
C. O. Lousto, J. Healy, and H. Nakano, Phys. Rev. **D93**, 044031 (2016), arXiv:1506.04768 [gr-qc].

Up-down spin configurations can be unstable (using low averaged PN)

D. Gerosa, M. Kesden, R. O'Shaughnessy, A. Klein, E. Berti, U. Sperhake, and D. Trifirò, Phys. Rev. Lett. **115**, 141102 (2015), arXiv:1506.09116 [gr-qc].

in between $r_{ud\pm} = (\sqrt{\alpha_2} \pm \sqrt{q\alpha_1})^4 M/(1-q)^2$.

We study the instability here by direct integration of the 3.5PN equations of motion and 2.5PN spins evolutions

C. O. Lousto and J. Healy, Phys. Rev. D **93**, 124074 (2016).

Beaconing binaries

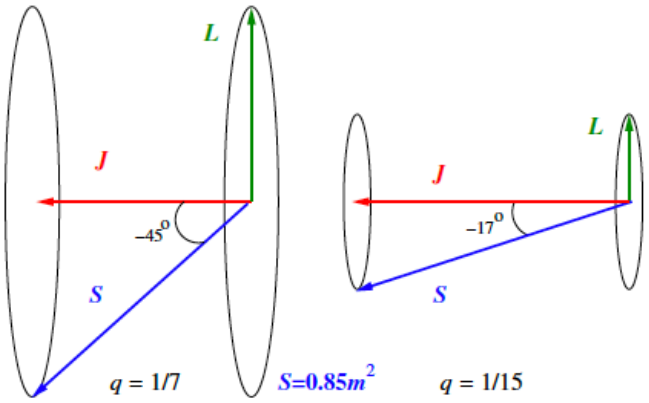

FIG. 1. Initial configuration of the orbital angular momentum $\vec{L}$, large hole spin $\vec{S}$, and total momentum of the system, $\vec{J}$. Both the spin and the orbital angular momentum precess (counter-clockwise) around $\vec{J}$ as the system evolves.

This configurations leads to an L-flip

In order to qualitatively understand the basic dependence of the beaconing phenomena on the binary parameters, we use a low order post-Newtonian analysis [see Eq. (3.2c) of Ref. [42]] with $\vec{S}_2 \cdot \hat{L} = -\vec{L} \cdot \hat{L}$ initially, to find a frequency of precession of $\vec{L}$:

$$M\Omega_L = 2\alpha_2^J/(1+q)^2(M/r)^3, \qquad (1)$$

where r is the coordinate separation of the holes, $\alpha_2^J = \vec{S}_2 \cdot \hat{J}/m_2^2$ the dimensionless spin of the large hole along $\vec{J}$ (perpendicular to $\vec{L}$), $M = m_1 + m_2$ the total mass of the system, and $q = m_1/m_2 \leq 1$ its mass ratio.

The critical separation radius r_c, characterizing the middle of the transitional precession, where the condition $S_2^L = \vec{S}_2 \cdot \hat{L} = -\vec{L} \cdot \hat{L} = -L$ is met is hence

$$(r_c/M)^{1/2} = (\alpha_2^L/2q)\left(1 + \sqrt{1 - 8(q/\alpha_2^L)^2}\right).$$

$q < 1/4$ for $r_c > 10M$

GW Beaconing and Polarization effects

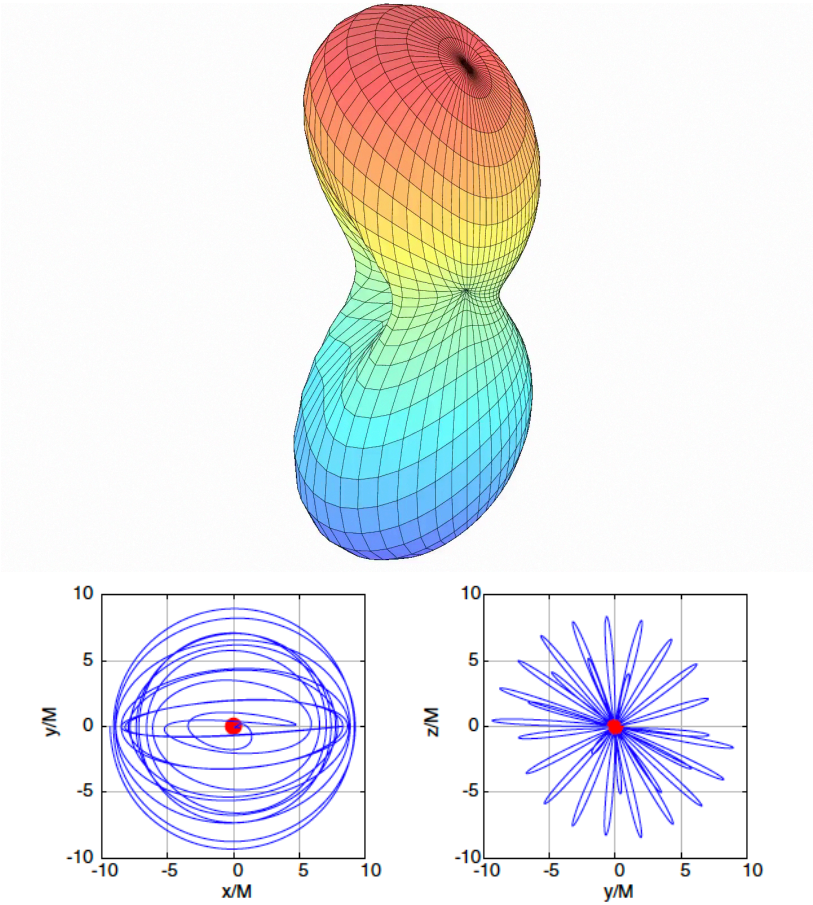

FIG. 5. The beaconing effect displayed by the power radiated for the binary case with mass ratio $q = 1/15$ as seen from the z axis (the initial direction of the orbital angular momentum) (above) and (below) the detail of the black hole trajectories in the initial orbital plane (left) and seen from an observer along the x axis (right).

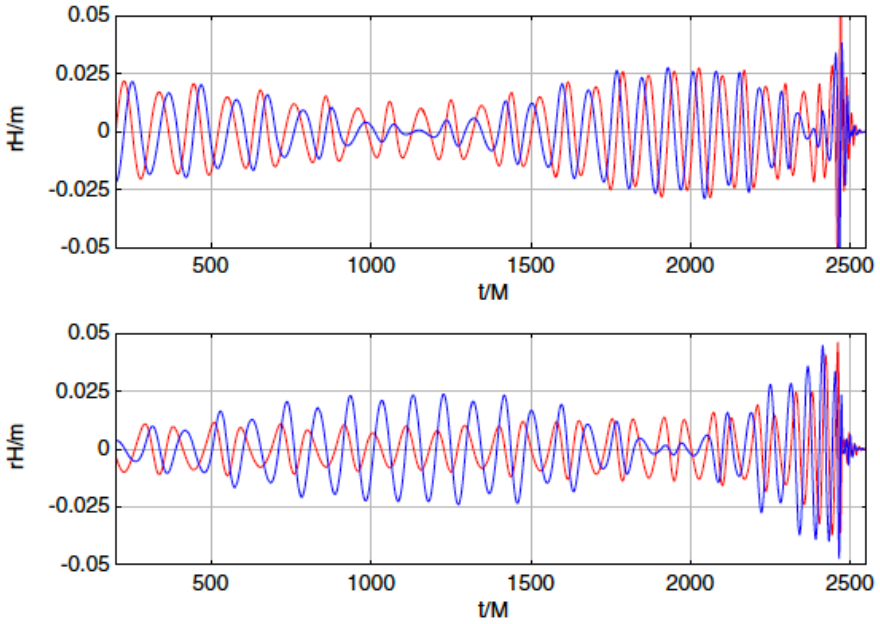

FIG. 4. The two polarizations of the waveform strain of the system with mass ratio $q = 1/15$ as seen from the z axis (the initial direction of the orbital angular momentum) (above) and the same waveform strain as seen from the y axis (below) reconstructed using modes up to $l_{\max} = 5$.

GW Beaconing and Polarization effects

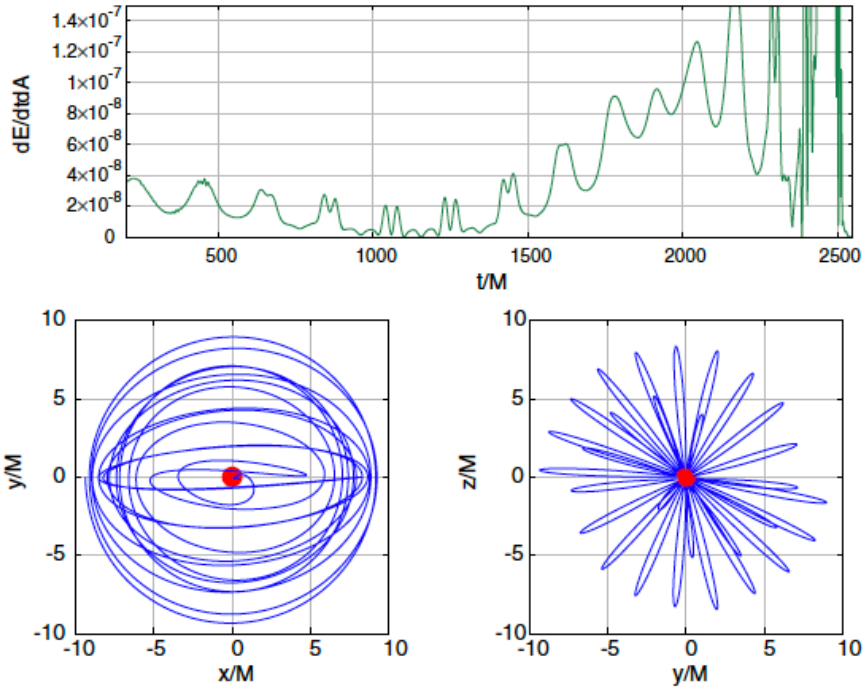

FIG. 5. The beaconing effect displayed by the power radiated for the binary case with mass ratio $q = 1/15$ as seen from the z axis (the initial direction of the orbital angular momentum) (above) and (below) the detail of the black hole trajectories in the initial orbital plane (left) and seen from an observer along the x axis (right).

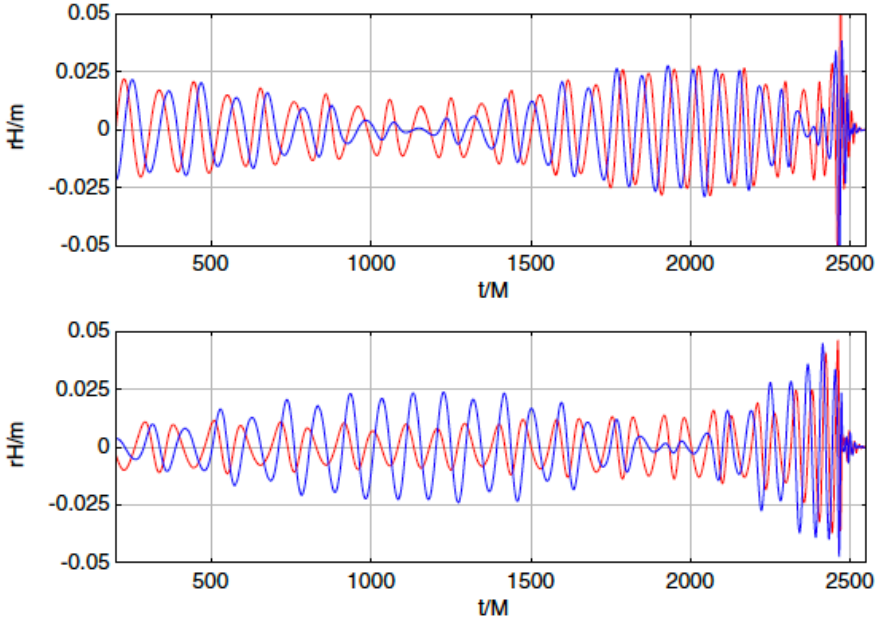

FIG. 4. The two polarizations of the waveform strain of the system with mass ratio $q = 1/15$ as seen from the z axis (the initial direction of the orbital angular momentum) (above) and the same waveform strain as seen from the y axis (below) reconstructed using modes up to $l_{\max} = 5$.

Observational consequences

- Beaconing effect likely for q < 1/4 and retrograde BBH systems
- Beaconing effect leads to higher chances of seeing a system face-on
- GW polarizations look like pretty different
  - Important to measure them
  - Relevant for LIGO, LISA and PTA merger observations

- When matter present, EM counterparts may have characteristic features on the beaconing frequency scale

➢ RIT GRMHD Simulation

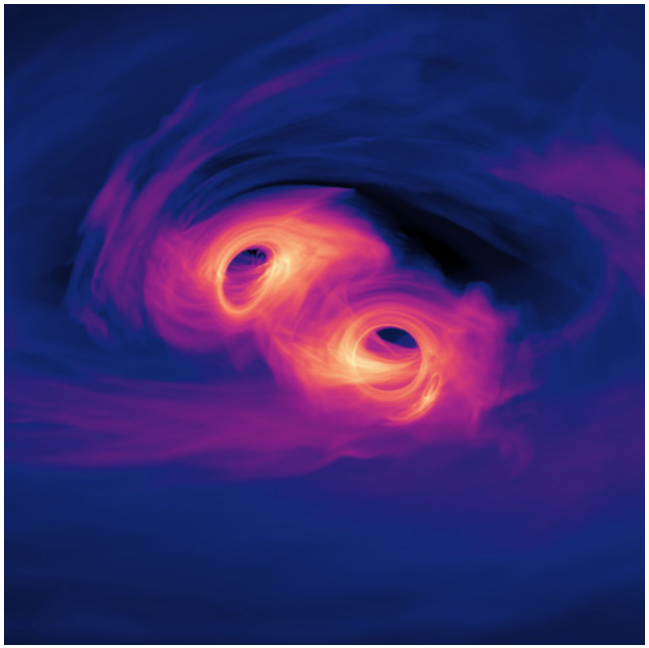

3. Merger Remnant

Merger Remnant

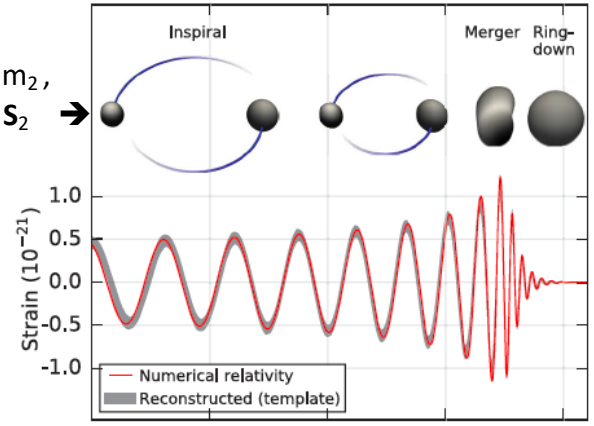

$m_1, m_2,$
$\mathbf{S}_1, \mathbf{S}_2$ ➔

➔ $M_f\ (q,\mathbf{S}_1,\mathbf{S}_2)$
$\mathbf{S}_f\ (q,\mathbf{S}_1,\mathbf{S}_2)$
$\mathbf{V}_f\ (q,\mathbf{S}_1,\mathbf{S}_2)$

➔ Lpeak
hpeak
fpeak

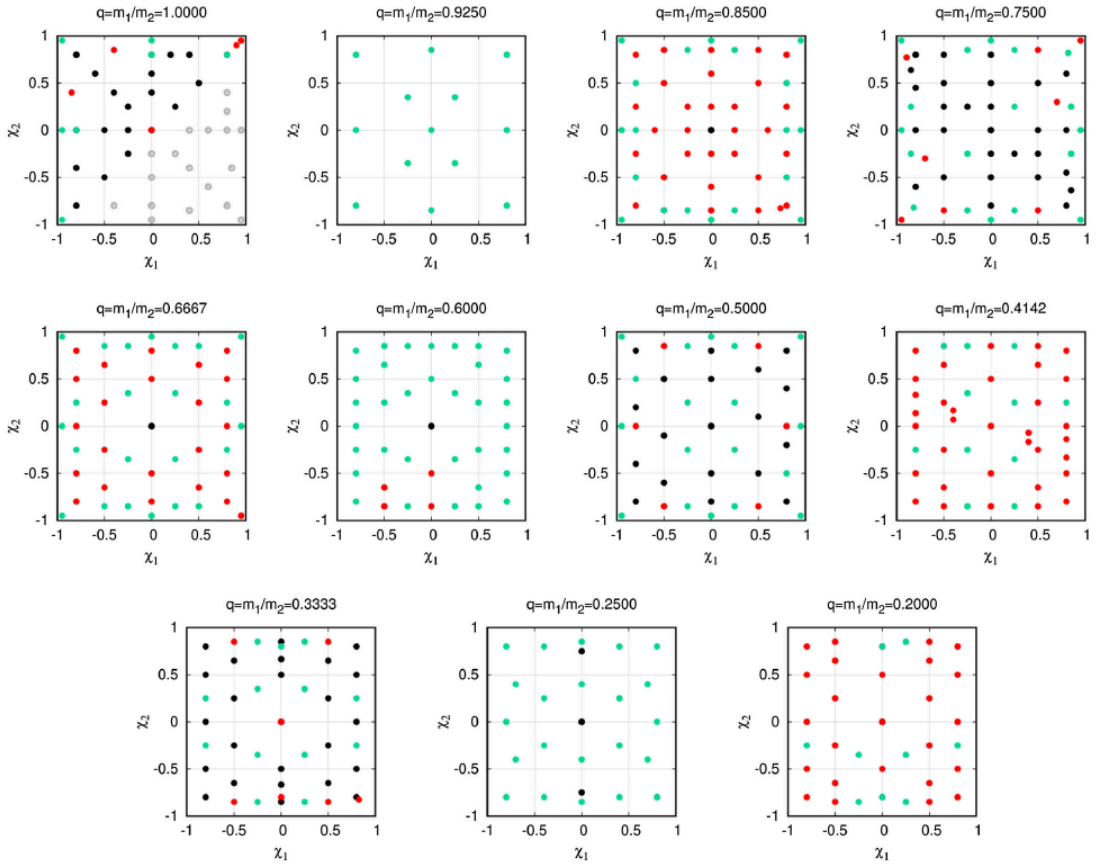

Simulations (3rd RIT Catalog)

- 477 aligned spin simulations
- $1/5 \le q \le 1$ and $-0.95 \le a_i \le +0.95$ for the spinning binaries
- $1/15 \le q < 1$ for the nonspinning binaries
- Runs give 10-20 orbits prior to merger at $e \approx 10^{-3}$

From: C.O.Lousto & J.Healy, Phys.Rev.D 102 (2020), 104018; Phys.Rev.D 100 (2019), 024021; Phys.Rev. D97 (2018), 084002.
There are many other different modeling in the literature.

Final remnant mass and spin modeling

$$\frac{M_{\rm rem}}{m} = (4\eta)^2\{M_0 + K_1\tilde{S}_\parallel + K_{2a}\tilde{\Delta}_\parallel\delta m + K_{2b}\tilde{S}_\parallel^2 + K_{2c}\tilde{\Delta}_\parallel^2 + K_{2d}\delta m^2 + K_{3a}\tilde{\Delta}_\parallel\tilde{S}_\parallel\delta m + K_{3b}\tilde{S}_\parallel\tilde{\Delta}_\parallel^2 + K_{3c}\tilde{S}_\parallel^3 + K_{3d}\tilde{S}_\parallel\delta m^2 + K_{4a}\tilde{\Delta}_\parallel\tilde{S}_\parallel^2\delta m + K_{4b}\tilde{\Delta}_\parallel^3\delta m + K_{4c}\tilde{\Delta}_\parallel^4 + K_{4d}\tilde{S}_\parallel^4 + K_{4e}\tilde{\Delta}_\parallel^2\tilde{S}_\parallel^2 + K_{4f}\delta m^4 + K_{4g}\tilde{\Delta}_\parallel\delta m^3 + K_{4h}\tilde{\Delta}_\parallel^2\delta m^2 + K_{4i}\tilde{S}_\parallel^2\delta m^2\} + [1 + \eta(\tilde{E}_{\rm ISCO} + 11)]\delta m^6,$$

where all 19 K_i are fitting parameters.

$$\alpha_{\rm rem} = \frac{S_{\rm rem}}{M_{\rm rem}^2} = (4\eta)^2\{L_0 + L_1\tilde{S}_\parallel + L_{2a}\tilde{\Delta}_\parallel\delta m + L_{2b}\tilde{S}_\parallel^2 + L_{2c}\tilde{\Delta}_\parallel^2 + L_{2d}\delta m^2 + L_{3a}\tilde{\Delta}_\parallel\tilde{S}_\parallel\delta m + L_{3b}\tilde{S}_\parallel\tilde{\Delta}_\parallel^2 + L_{3c}\tilde{S}_\parallel^3 + L_{3d}\tilde{S}_\parallel\delta m^2 + L_{4a}\tilde{\Delta}_\parallel\tilde{S}_\parallel^2\delta m + L_{4b}\tilde{\Delta}_\parallel^3\delta m + L_{4c}\tilde{\Delta}_\parallel^4 + L_{4d}\tilde{S}_\parallel^4 + L_{4e}\tilde{\Delta}_\parallel^2\tilde{S}_\parallel^2 + L_{4f}\delta m^4 + L_{4g}\tilde{\Delta}_\parallel\delta m^3 + L_{4h}\tilde{\Delta}_\parallel^2\delta m^2 + L_{4i}\tilde{S}_\parallel^2\delta m^2\} + \tilde{S}_\parallel(1 + 8\eta)\delta m^4 + \eta\tilde{J}_{\rm ISCO}\delta m^6,$$

where the 19 L_i are fitting parameters.

(Note that the two formulas, for the the final mass and final spin impose the particle limit through their ISCO contributions).

where

$$m = m_1 + m_2,$$
$$\delta m = \frac{m_1 - m_2}{m},$$
$$\tilde{S} = (\vec{S}_1 + \vec{S}_2)/m^2,$$
$$\tilde{\Delta} = (\vec{S}_2/m_2 - \vec{S}_1/m_1)/m,$$

where m_i is the mass of BH $i = 1, 2$ and $\vec{S}_i$ is the spin of BH i. We also use the auxiliary variables

and

$$\eta = \frac{m_1 m_2}{m^2},$$
$$q = \frac{m_1}{m_2},$$
$$\vec{\alpha}_i = \vec{S}_i/m_i^2,$$

where $|\vec{\alpha}_i| \leq 1$ is the dimensionless spin of BH i, and we use the convention that $m_1 \leq m_2$ and hence $q \leq 1$. Here the index $\perp$ and $\parallel$ refer to components perpendicular to and parallel to the orbital angular momentum.

Recoil velocity and stats

We model the in-plane recoil as

$$\vec{V}_{\rm recoil}(q,\vec{\alpha}_i) = v_m \hat{e}_1 + v_\perp(\cos(\xi)\hat{e}_1 + \sin(\xi)\hat{e}_2),$$

where $\hat{e}_1$, $\hat{e}_2$ are orthogonal unit vectors in the orbital plane, and ξ measures the angle between the "unequal mass" and "spin" contributions to the recoil velocity in the orbital plane, and with,

$$\begin{aligned} v_\perp = {} & H\eta^2(\tilde{\Delta}_\parallel + H_{2a}\tilde{S}_\parallel \delta m + H_{2b}\tilde{\Delta}_\parallel \tilde{S}_\parallel + H_{3a}\tilde{\Delta}_\parallel^2 \delta m \\ & + H_{3b}\tilde{S}_\parallel^2 \delta m + H_{3c}\tilde{\Delta}_\parallel \tilde{S}_\parallel^2 + H_{3d}\tilde{\Delta}_\parallel^3 \\ & + H_{3e}\tilde{\Delta}_\parallel \delta m^2 + H_{4a}\tilde{S}_\parallel \tilde{\Delta}_\parallel^2 \delta m + H_{4b}\tilde{S}_\parallel^3 \delta m \\ & + H_{4c}\tilde{S}_\parallel \delta m^3 + H_{4d}\tilde{\Delta}_\parallel \tilde{S}_\parallel \delta m^2 \\ & + H_{4e}\tilde{\Delta}_\parallel \tilde{S}_\parallel^3 + H_{4f}\tilde{S}_\parallel \tilde{\Delta}_\parallel^3), \\ \xi = {} & a + b\tilde{S}_\parallel + c\delta m \tilde{\Delta}_\parallel, \end{aligned} \tag{25}$$

where

$$v_m = \eta^2 \delta m (A + B\delta m^2 + C\delta m^4) \tag{26}$$

and according to Ref. [48] we have $A = -8712$, and $B = -6516$ and $C = 3907$ km/s.

[48] J. Healy, C. O. Lousto, and Y. Zlochower, Phys. Rev. D **96**, 024031 (2017).

TABLE IV. Fitting statistics for remnant formulas presented here.

Value	$M_{\rm rem}/m$	$\alpha_{\rm rem}$	Recoil (km/s)
RMS	2.62396×10^{-4}	7.90772×10^{-4}	3.48
Std. Dev.	2.52011×10^{-4}	7.58235×10^{-4}	3.31
Avg. Diff.	-6.38437×10^{-6}	4.33099×10^{-4}	0.21
Max Diff.	1.19201×10^{-3}	2.59799×10^{-3}	10.98
Min Diff.	-1.13027×10^{-3}	-2.45274×10^{-3}	−12.73

These expressions can be generalized to precessing binaries

Lousto & Zlochower, Phys.Rev. D89 (2014) , 104052
Phys.Rev. D92 (2015), 024022

Peak luminosity, amplitude, and frequency modeling

$$
\begin{aligned}
L_{\rm peak} = (4\eta)^2\{&N_0 + N_1\tilde{S}_\parallel + N_{2a}\tilde{\Delta}_\parallel\delta m \\
&+ N_{2b}\tilde{S}_\parallel^2 + N_{2c}\tilde{\Delta}_\parallel^2 + N_{2d}\delta m^2 \\
&+ N_{3a}\tilde{\Delta}_\parallel\tilde{S}_\parallel\delta m + N_{3b}\tilde{S}_\parallel\tilde{\Delta}_\parallel^2 + N_{3c}\tilde{S}_\parallel^3 \\
&+ N_{3d}\tilde{S}_\parallel\delta m^2 + N_{4a}\tilde{\Delta}_\parallel\tilde{S}_\parallel^2\delta m \\
&+ N_{4b}\tilde{\Delta}_\parallel^3\delta m + N_{4c}\tilde{\Delta}_\parallel^4 + N_{4d}\tilde{S}_\parallel^4 \\
&+ N_{4e}\tilde{\Delta}_\parallel^2\tilde{S}_\parallel^2 + N_{4f}\delta m^4 + N_{4g}\tilde{\Delta}_\parallel\delta m^3 \\
&+ N_{4h}\tilde{\Delta}_\parallel^2\delta m^2 + N_{4i}\tilde{S}_\parallel^2\delta m^2\},
\end{aligned}
$$

where all N_i are fitting parameters

$$
\begin{aligned}
(r/m)h_{22}^{\rm peak} = (4\eta)\{&H_0 + H_1\tilde{S}_\parallel + H_{2a}\tilde{\Delta}_\parallel\delta m \\
&+ H_{2b}\tilde{S}_\parallel^2 + H_{2c}\tilde{\Delta}_\parallel^2 + H_{2d}\delta m^2 \\
&+ H_{3a}\tilde{\Delta}_\parallel\tilde{S}_\parallel\delta m + H_{3b}\tilde{S}_\parallel\tilde{\Delta}_\parallel^2 + H_{3c}\tilde{S}_\parallel^3 \\
&+ H_{3d}\tilde{S}_\parallel\delta m^2 + H_{4a}\tilde{\Delta}_\parallel\tilde{S}_\parallel^2\delta m \\
&+ H_{4b}\tilde{\Delta}_\parallel^3\delta m + H_{4c}\tilde{\Delta}_\parallel^4 + H_{4d}\tilde{S}_\parallel^4 \\
&+ H_{4e}\tilde{\Delta}_\parallel^2\tilde{S}_\parallel^2 + H_{4f}\delta m^4 + H_{4g}\tilde{\Delta}_\parallel\delta m^3 \\
&+ H_{4h}\tilde{\Delta}_\parallel^2\delta m^2 + H_{4i}\tilde{S}_\parallel^2\delta m^2\},
\end{aligned}
$$

where all of the H_i are fitting parameters.

$$
\begin{aligned}
m\omega_{22}^{\rm peak} = \{&W_0 + W_1\tilde{S}_\parallel + W_{2a}\tilde{\Delta}_\parallel\delta m \\
&+ W_{2b}\tilde{S}_\parallel^2 + W_{2c}\tilde{\Delta}_\parallel^2 + W_{2d}\delta m^2 \\
&+ W_{3a}\tilde{\Delta}_\parallel\tilde{S}_\parallel\delta m + W_{3b}\tilde{S}_\parallel\tilde{\Delta}_\parallel^2 + W_{3c}\tilde{S}_\parallel^3 \\
&+ W_{3d}\tilde{S}_\parallel\delta m^2 + W_{4a}\tilde{\Delta}_\parallel\tilde{S}_\parallel^2\delta m \\
&+ W_{4b}\tilde{\Delta}_\parallel^3\delta m + W_{4c}\tilde{\Delta}_\parallel^4 + W_{4d}\tilde{S}_\parallel^4 \\
&+ W_{4e}\tilde{\Delta}_\parallel^2\tilde{S}_\parallel^2 + W_{4f}\delta m^4 + W_{4g}\tilde{\Delta}_\parallel\delta m^3 \\
&+ W_{4h}\tilde{\Delta}_\parallel^2\delta m^2 + W_{4i}\tilde{S}_\parallel^2\delta m^2\},
\end{aligned}
$$

where all of the W_i are fitting parameters.

TABLE III. Fitting statistics for peak luminosity, frequency and amplitude of the mode (2,2) formulae

Value	Peak Luminosity	Peak $m\omega_{22}$	Peak $(r/m)h_{22}$
RMS	1.68809e-05	5.95755e-03	1.54105e-03
Std. Dev.	1.46664e-05	5.70386e-03	1.47523e-03
Avg. Diff.	6.77198e-06	2.70026e-05	-2.44938e-05
Max Diff.	7.18966e-05	2.63070e-02	8.39437e-03
Min Diff.	-3.18964e-05	-3.94535e-02	-4.81573e-03

Ready for direct applications to GW remnants, Tests of Gravity, astrophysics, and cosmology (merger trees).

Hangup revisited: Unequal masses

We will study the hangup dependence of those 181 simulations on the variable

$$\frac{1}{1-C}S_{\rm hu} = (\vec{S}\cdot\hat{L} + C\delta m\vec{\Delta}\cdot\hat{L}), \qquad (10)$$

where C will be the fitting parameter that regulates the coupling to the total spin $\vec{S}$ with the "delta" combination $\delta m\vec{\Delta}$.

$$\eta[N-N_0] = D + AS_{\rm hu} + BS_{\rm hu}^2, \qquad (11)$$

are presented in Fig. 2. This shows the dependence of the hangup effect with respect to the nonspinning binaries. We see that this dependence can be expressed in terms of the spin variable

$$\frac{3}{2}S_{\rm hu} = \left(\vec{S}\cdot\hat{L} + \frac{1}{3}\delta m\vec{\Delta}\cdot\hat{L}\right), \qquad (12)$$

to an excellent degree of approximation since $C = 0.3347$ from the fits.

TABLE I. RMS and variance of S_0, $S_{\rm eff}$, and $S_{\rm hu}$ fits. Here we show ndf (no. degrees of freedom), WSSR = weighted sum of the residuals, RMS $= \sqrt{\rm WSSR/ndf}$, and Variance = reduced χ^2 = WSSR/ndf.

Variable	Coefficient	ndf	WSSR	RMS	Variance
S_0	0.5	167	0.702	0.065	0.0042
$S_{\rm eff}$	0.428571	167	0.361	0.047	0.0022
$S_{\rm PN}$	0.398936	167	0.281	0.041	0.0017
$S_{\rm hu}$	0.333333	167	0.214	0.036	0.0013

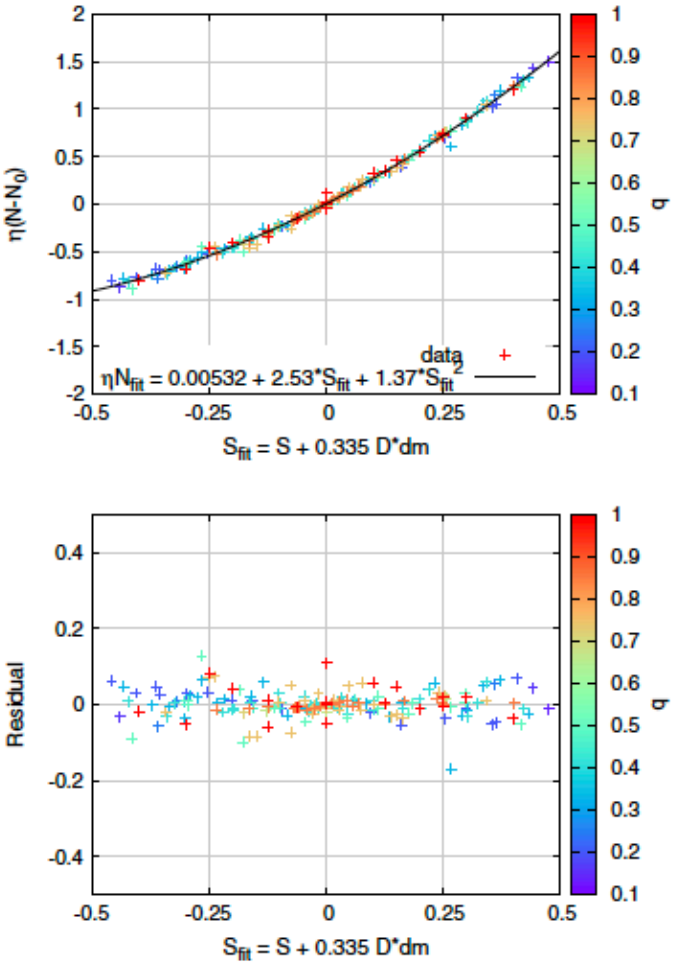

FIG. 2. The difference in number of orbits with respect to the nonspinning case for full numerical binary black hole mergers. We use the (2,2) mode of the waveform and calculate the number of cycles between $m\omega = 0.07$ and $m\omega_{\rm peak}$. We study in detail the cases with $q = 1.00$, $q = 0.85$, $q = 0.75$, $q = 0.4142$, $q = 0.50$, $q = 0.333$ and $q = 0.20$ and fit a quadratic dependence with the spin variables to extract the linear spin coefficients of $\vec{S}\cdot\hat{L} + C\delta m\vec{\Delta}\cdot\hat{L}$. The residuals of such a fit are also displayed showing no systematics.

$S_{\rm hu}$ perhaps a better spin variable for waveform modeling

4. Merger Recoils

Gravitational Radiation Recoil

• In binary black-hole (BH) coalescences, asymmetrical gravitational radiation carries a net linear momentum, causing center-of-mass recoil. To conserve momentum the merged BH is given a kick in the opposite direction.

• The magnitude of the kick has an impact in astrophysics:
  - galactic population synthesis models
  - massive black hole formation scenarios

• If large enough (compared to escape velocity), the final BH remnant could be kicked out from the host structure …

• Escape velocities:
  < 100 km/so for globular clusters
  ~ 500-1000 km/s for spiral galaxy bulges
  ~ 2000 km/s for giant elliptical galaxies

• There are a number of possible observational consequences: off-set galactic nuclei, displaced active galactic nuclei, population of galaxies without SMBHs, x-rays afterglows, feedback trails.

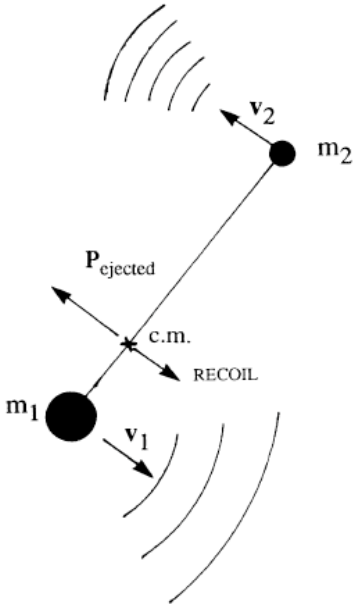

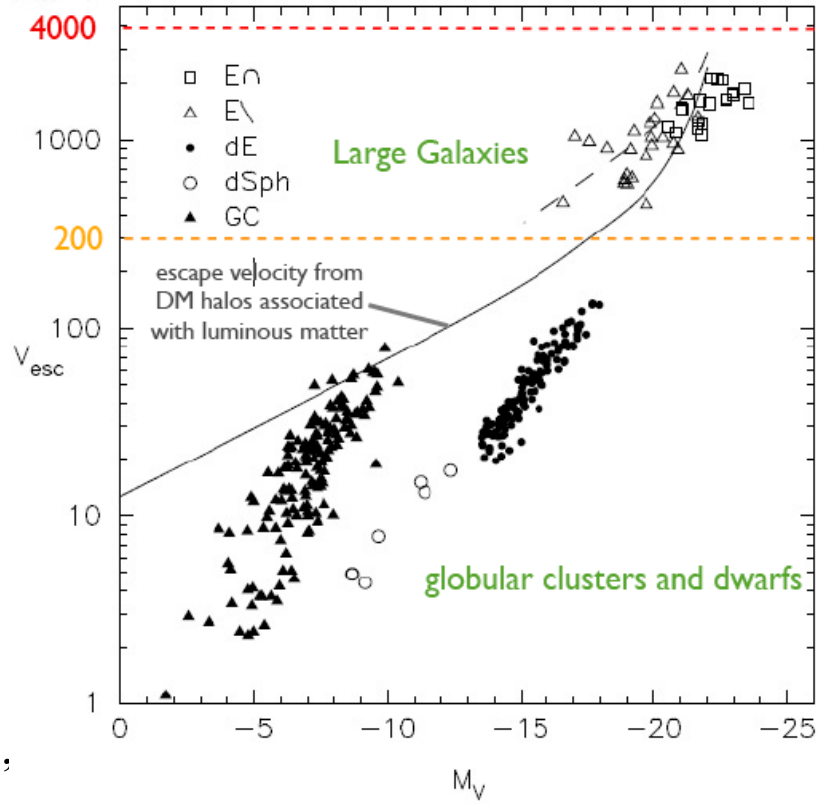

Hangup Recoils

- When spins are aligned with L, repulsive spin-orbit coupling delays the merger (orbital-hangup effect), maximizing the amplitude of gravitational radiation (up to 10%) [Campanelli+ 06].
- Combined with the superkick effect [Campanelli+ 07].(which maximizes the asymmetry of momentum radiated), this leads to very large recoils [Lousto & Zlochower, PRL, 2011].

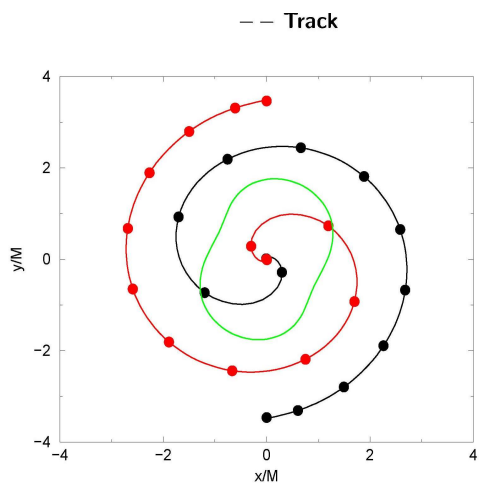

Figure 4: Puncture tracks for the – – configuration.

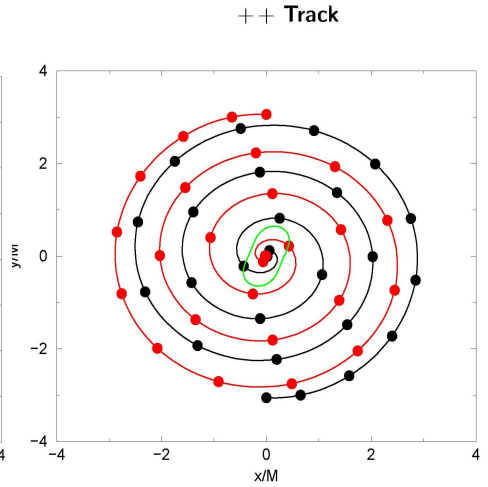

Figure 6: Puncture tracks for the + + configuration.

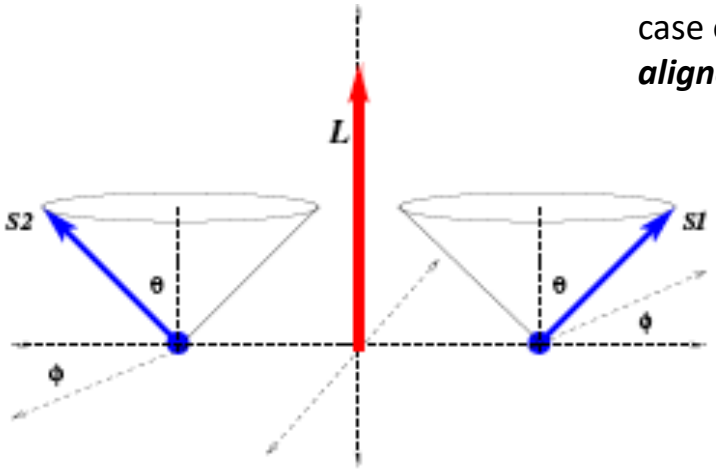

Three parameters family of initial configurations depending of ϕ, θ, and spin magnitude, a. Each dot in the plot are 6- runs to span the ϕ dependence. 48 new runs.

Peak occurs at 5000 km/s in the case of ***nearly aligned spins***

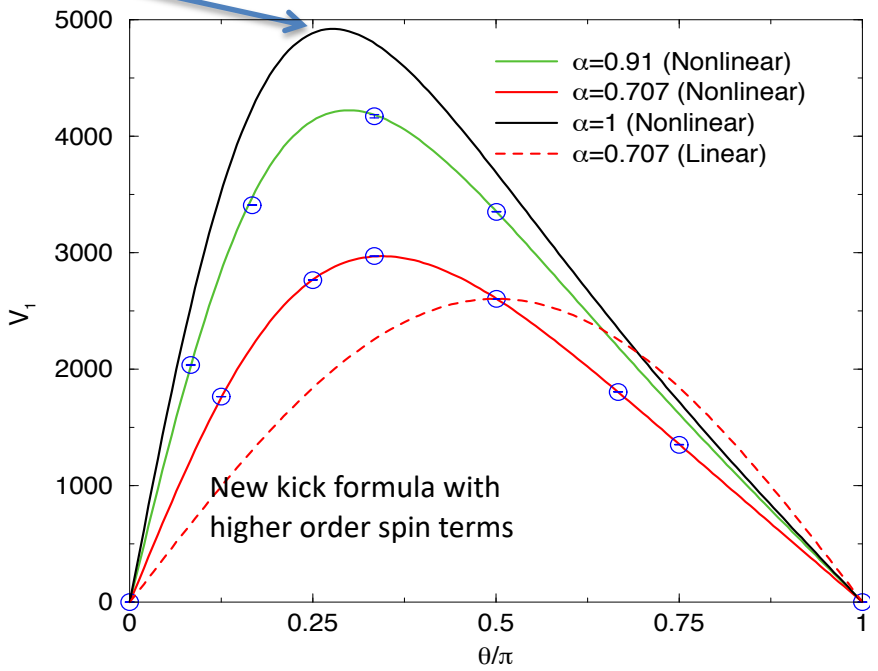

Probabilities to observe large recoils

Partial alignment of the spins by gas accretion cannot inhibit large recoils as conjectured in [Bogdanovic+07), Dotti+10)]

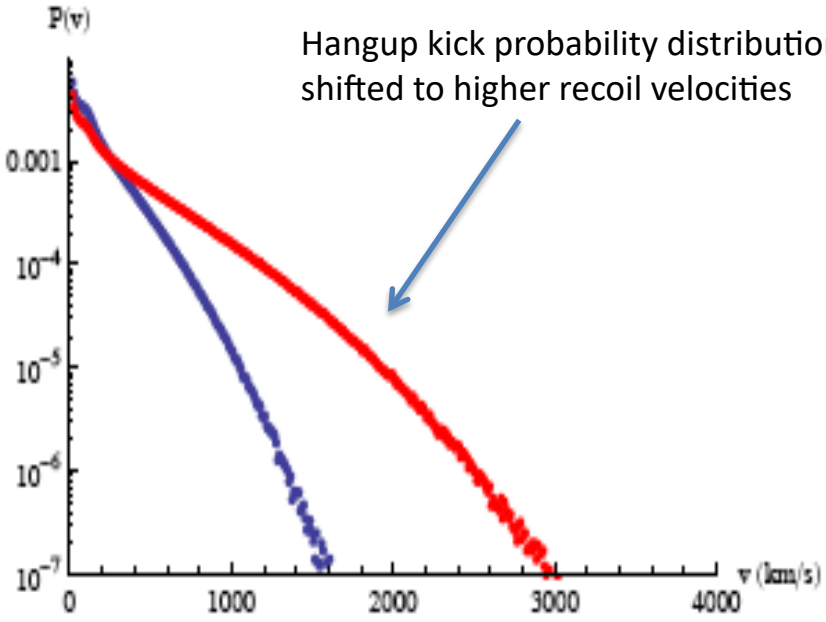

Hangup kick probability distribution shifted to higher recoil velocities

Spin distribution: $P(x) \propto (1-x)^{(b-1)} x^{(a-1)}$

Mass distribution: $P(q) \propto q^{-0.3}(1-q)$

Feed this to recoil velocity formula and calculate the recoil distribution (table).

Probabilities that remnant BH recoils in any direction from host structure (spins from SPH simulations of hot and cold accretion models) [Lousto+12]:

- 0.02% for galaxies with v_{esc} ~ 2500 km/s
- 5% for galaxies with v_{esc} ~1000 km/s
- 20% for galaxies with v_{esc} ~500 km/s

For the hot case, there is a nontrivial probability of observing a recoil larger than 2000 km/s, but for cold disks, such recoils are suppressed.

Vel. (km s^{-1})	(Hot)	Obs. (Hot)	(Cold)	Obs. (Cold)
0-100	34.2593 %	60.1847 %	41.4482 %	71.2967 %
100-200	21.1364 %	16.9736 %	28.3502 %	16.8471 %
200-300	11.6901 %	8.1110 %	12.503 %	6.1508 %
300-400	7.8400 %	4.8108 %	7.0967 %	2.8281 %
400-500	5.7590 %	3.0913 %	4.2490 %	1.3973 %
500-1000	14.0283 %	5.6593 %	5.9309 %	1.4258 %
1000-1500	4.0183 %	0.9809 %	0.4030 %	0.0526 %
1500-2000	1.0309 %	0.1638 %	0.0185 %	0.0015 %
2000-2500	0.2047 %	0.0223 %	0.0005 %	2×10^{-5}%
2500-3000	0.0296 %	0.0023 %	1×10^{-5}%	0.%
3000-3500	0.0032 %	0.0002 %	0. %	0.%
3500-4000	0.0002 %	$4. \times 10^{-6}$ %	0.% %	0.%

Angular distributions of Recoils

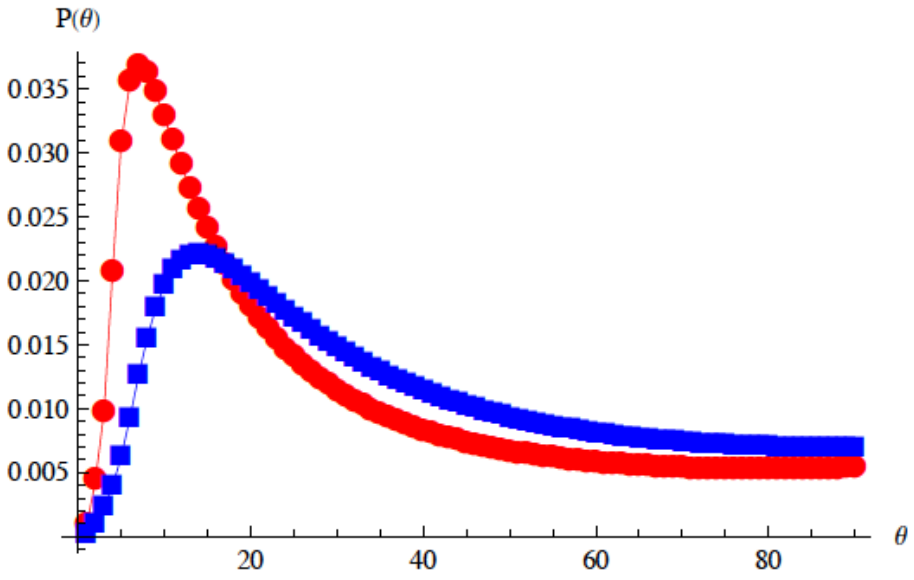

FIG. 11: The probability distribution of the inclination angle θ of the recoil (measured with respect to the axis of the angular momentum) for hot (narrower distribution, red circles) and cold environments (blue squares). Angles are measured in degrees. Note that $P(180^\circ - \theta) = P(\theta)$. These distributions were created by mapping $\theta \rightarrow 180^\circ - \theta$ for $\theta > 90^\circ$.

TABLE X: Maximum recoil angle θ (angle with respect to the orbital angular momentum axis) for given recoil velocity ranges. Note here that $\theta_{\rm max} < \delta$ means that θ must smaller than δ or larger than $180^\circ - \delta$.

Range	$\theta_{\rm max}$ (Hot)	$\theta_{\rm max}$ (Cold)
$0 - 100$ km s^{-1}	90°	90°
$100 - 200$ km s^{-1}	90°	90°
$200 - 300$ km s^{-1}	$< 80^\circ$	$< 70^\circ$
$300 - 400$ km s^{-1}	$< 45^\circ$	$< 40^\circ$
$400 - 500$ km s^{-1}	$< 33^\circ$	$< 30^\circ$
$500 - 600$ km s^{-1}	$< 25^\circ$	$< 21^\circ$
$500 - 1000$ km s^{-1}	$< 25^\circ$	$< 21^\circ$
$1000 - 1500$ km s^{-1}	$< 11^\circ$	$< 8^\circ$
$1500 - 2000$ km s^{-1}	$< 7^\circ$	$< 5^\circ$
$2000 - 2500$ km s^{-1}	$< 5^\circ$	$< 4^\circ$
$2500 - 3000$ km s^{-1}	$< 4^\circ$	$< 2^\circ$
$3000 - 3500$ km s^{-1}	$< 3^\circ$	***

Black holes kicks and post post merger signatures

- Recoiling BHs can retain a massive accretion disk. The disk will fuel a lasting QSO phase while the BH wanders far from the galactic nucleus.
- There are relatively few observations of kick candidates:

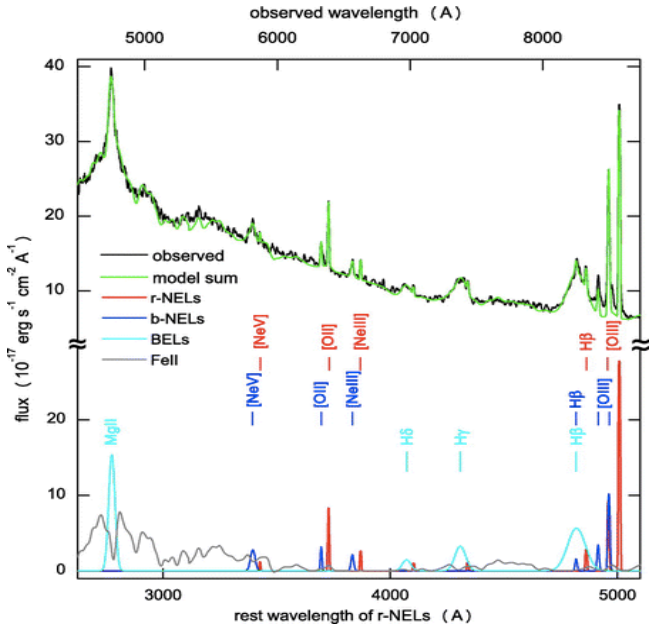

- SDSS J0927 + 2943 [Komossa et al. 2008]
  - BLR (one set) shifted 2600 km/s; double picked NLR
  - Kick interpretation: blue system is kicked hole, with blue NLR due to expanding gas from edge of bound disk. Red NLR is in host galaxy ionized by kicked AGN.

- More double-peaked emitters [Bonning et al, 2007; SDSSJ1050 Shields et al, 2009; Civano et al, 2010]

- Alternative interpretations: binary BHs, unusual NLR properties

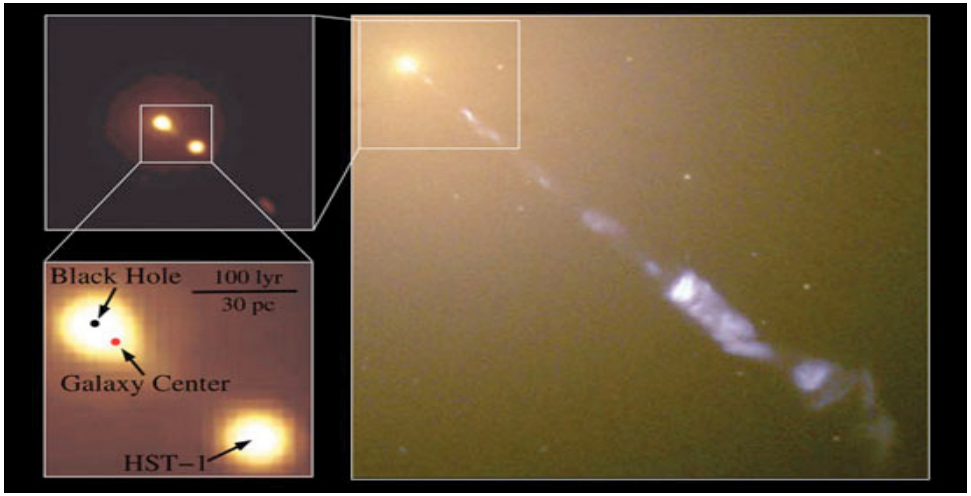

- HST image of a displaced SMBH in M87 [Batchelor et al, ApJL 2010]; Kick due postmerger ot jet?

- More off-set nuclei [Barth et al. 2008]

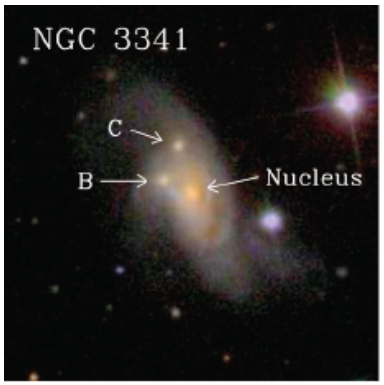

The puzzling case of the radio-loud QSO 3C 186: a gravitational wave recoiling black hole in a young radio source?

M. Chiaberge[1,2], J. C. Ely[1], E. T. Meyer[3], M. Georganopoulos[3,4], A. Marinucci[5], S. Bianchi[5], G. R. Tremblay[6], B. Hilbert[1], J. P. Kotyla[1], A. Capetti[7], S. A. Baum[8,9], F. D. Macchetto[1], G. Miley[10], C. P. O'Dea[8,9], E. S. Perlman[11], W. B. Sparks[1], and C. Norman[1,2]

Results. HST imaging shows that the active nucleus is offset by 1.3 ± 0.1 arcsec (i.e. ~11 kpc) with respect to the center of the host galaxy. Spectroscopic data show that the broad emission lines are offset by −2140 ± 390 km s^{-1} with respect to the narrow lines. Velocity shifts are often seen in QSO spectra, in particular in high-ionization broad emission lines. The host galaxy of the quasar displays a distorted morphology with possible tidal features that are typical of the late stages of a galaxy merger.
Conclusions. A number of scenarios can be envisaged to account for the observed features. While the presence of a peculiar outflow cannot be completely ruled out, all of the observed features are consistent with those expected if the QSO is associated with a gravitational wave (GW) recoiling BH. Future detailed studies of this object will allow us to confirm this type of scenario and will enable a better understanding of both the physics of BH-BH mergers and the phenomena associated with the emission of GW from astrophysical sources.

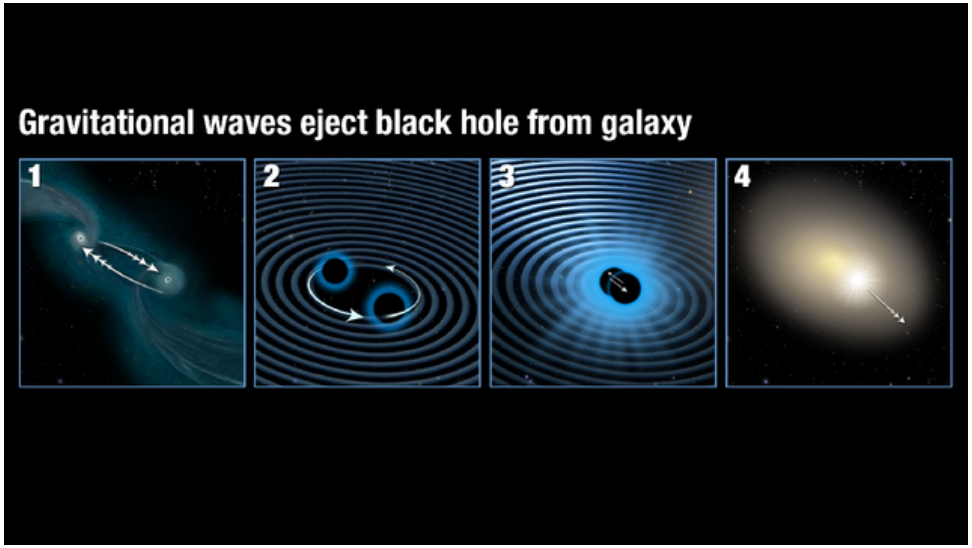

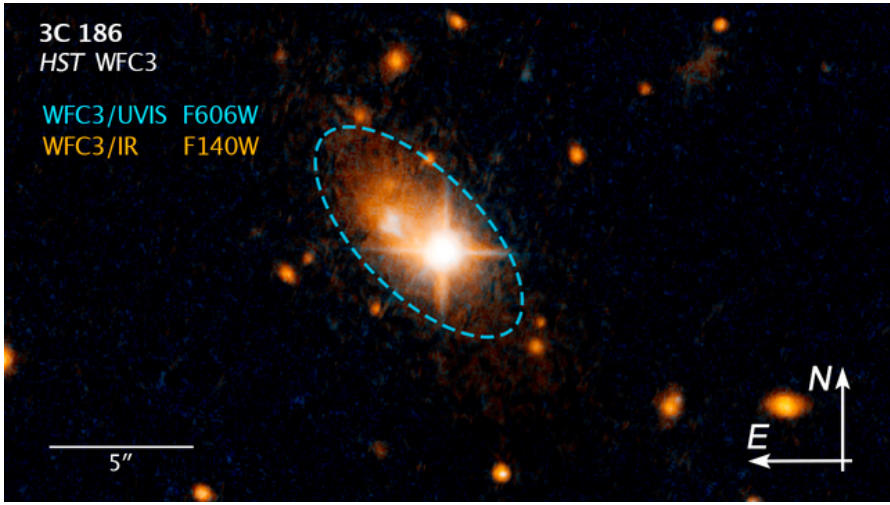

M.Chiaberge et al. Astron.Astrophys. 600 (2017) A57 and its followup: Astrophys.J. 861 (2018) , 56
``The Recoiling Black Hole Candidate 3C 186: Spatially Resolved Quasar Feedback and Further Evidence of a Blueshifted Broad-line Region''

Solving the inverse recoil problem

MODELING THE BLACK HOLE MERGER OF QSO 3C 186

CARLOS O.LOUSTO, YOSEF ZLOCHOWER, AND MANUELA CAMPANELLI

Spin magnitude and directions priors

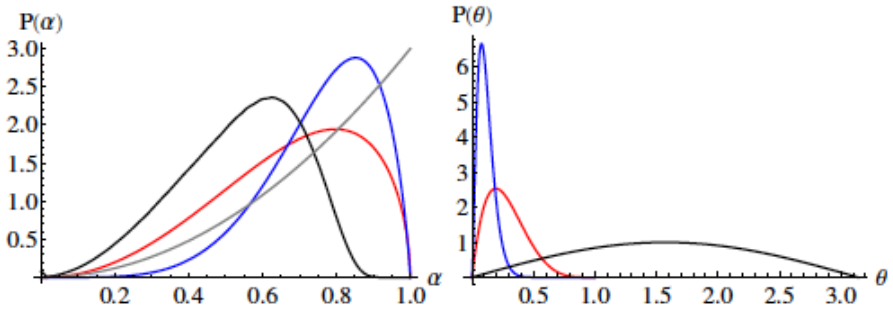

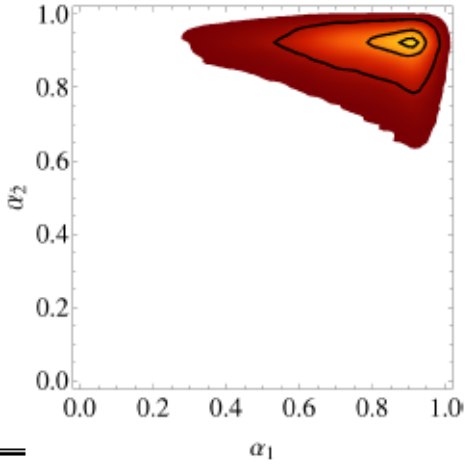

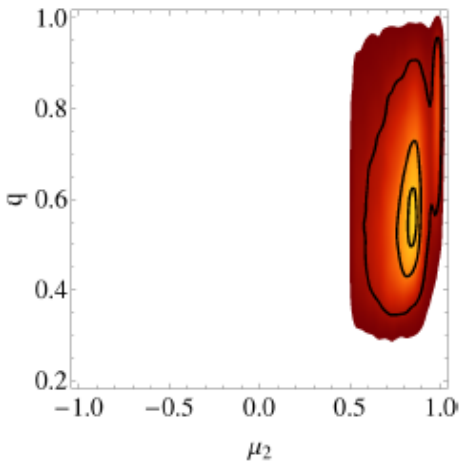

Binary parameters for producing Vrecoil>2,000km/s

	μ_1	μ_2	α_1	α_2	q
Cold	$1.00^{+0}_{-0.02}$	$0.86^{+0.14}_{-0.18}$	$0.93^{+0.05}_{-0.31}$	$0.93^{+0.06}_{-0.10}$	$0.58^{+0.39}_{-0.19}$
Hot	$0.97^{+0.02}_{-0.08}$	$0.89^{+0.08}_{-0.14}$	$0.91^{+0.06}_{-0.36}$	$0.93^{+0.04}_{-0.14}$	$0.59^{+0.30}_{-0.18}$
Dry	$0.09^{+0.70}_{-0.08}$	$0.57^{+0.24}_{-0.48}$	$0.67^{+0.14}_{-0.20}$	$0.75^{+0.08}_{-0.14}$	$0.61^{+0.24}_{-0.18}$
Uni.	$0.45^{+0.50}_{-0.44}$	$0.57^{+0.32}_{-0.48}$	$0.99^{+0}_{-0.46}$	$0.99^{+0}_{-0.26}$	$0.49^{+0.26}_{-0.18}$

	$\alpha_{\rm final}$	$\delta M\%$	P_{2000}	P_{2500}	P_{3000}
Cold	$0.91^{+0.02}_{-0.05}$	$8.6^{+1.0}_{-1.8}$	0.048%	0.0045%	0.00034%
Hot	$0.89^{+0.04}_{-0.04}$	$8.1^{+1.4}_{-1.4}$	0.157%	0.021%	0.0018%
Dry	$0.73^{+0.08}_{-0.10}$	$5.4^{+1.1}_{-0.8}$	0.229%	0.021%	0.00071%
Uni.	$0.75^{+0.10}_{-0.18}$	$5.6^{+1.7}_{-1.4}$	2.130%	0.694%	0.18%

Binary spins and mass ratio (q>1/4)
(displayed for the cold accretion model)

Remnant spin and radiated mass
(for the cold accretion model)

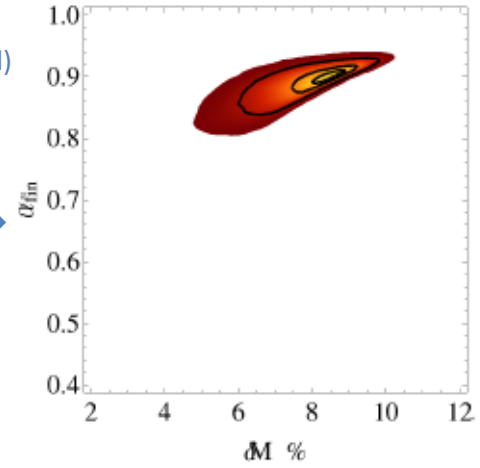

- Published in Astrophys.J. 841 (2017), L28

Solving accretion history

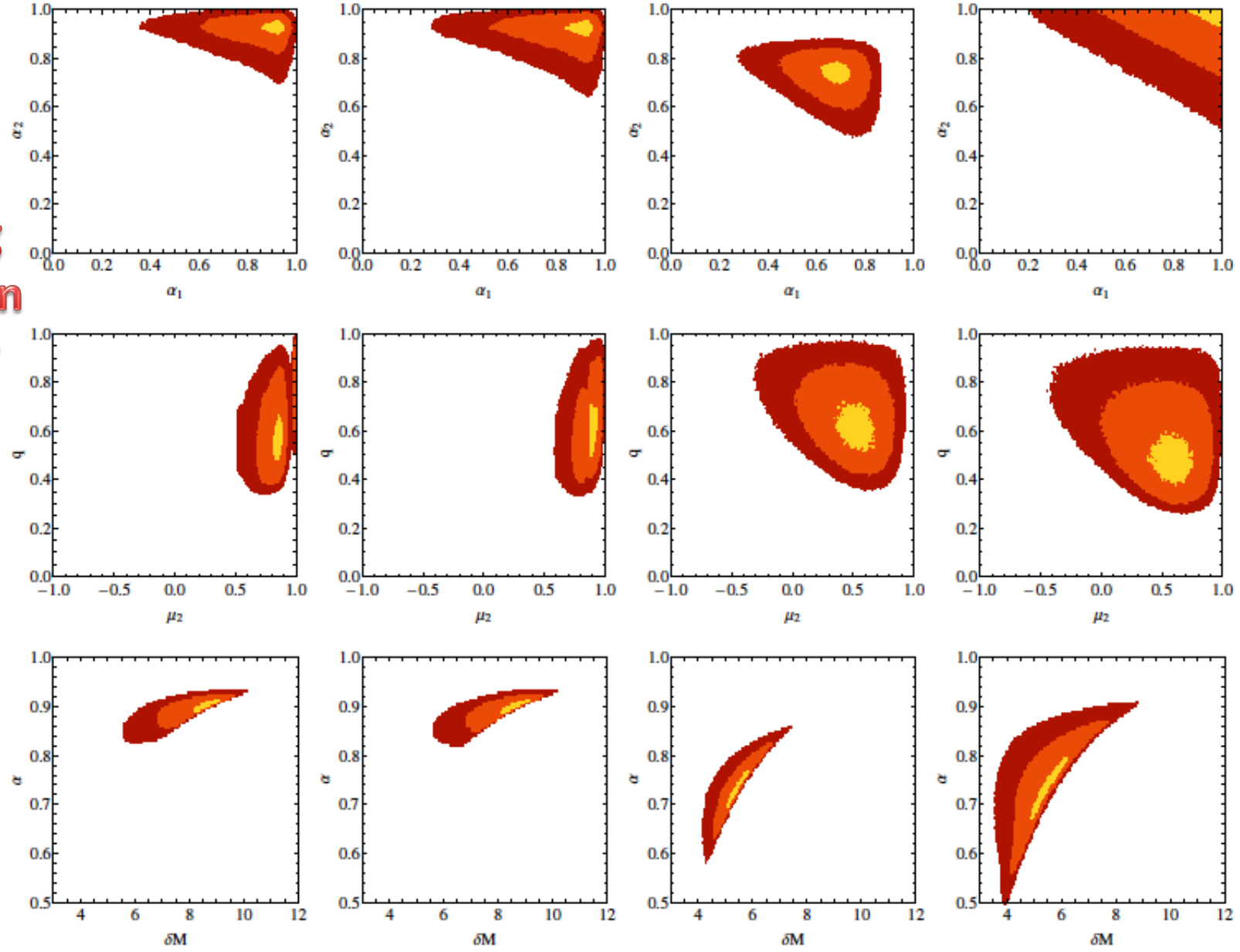

Figure 2. Histograms of the relative probabilities for the parameters of the progenitor and remnant given a recoil of 2000 km/s or larger assuming the the binary's parameters resulted from (arranged left to right) cold accretion, hot accretion, randomly oriented spins with spin magnitudes based on a dry merger model, and a uniform distribution in spin magnitudes and directions. In each panel the yellow region denotes the top 10% bins, orange denotes the top 68% bins, and red denotes the top 95% bins. The parameters are the spin magnitudes α_1 and α_2; polar orientation (of the larger BH) $\mu_2 = \cos\theta_2$; mass ratio q; total radiated mass δM; and final spin magnitude α.

A target for Pulsar Timing

- ✓ Case study 3C 186: z=1, $6 \times 10^9 M_{sun}$
  - We have a fair idea of S_1, S_2, and q
    (q > 1/4 and a > 0.8 compatible with obs.)
  - NR waveform run for 20,000M
    (18 years! ~ a cycle per month)
  - Amplitude of GW h ~ 10^{-14}
  - Need daily follow-ups of PT!

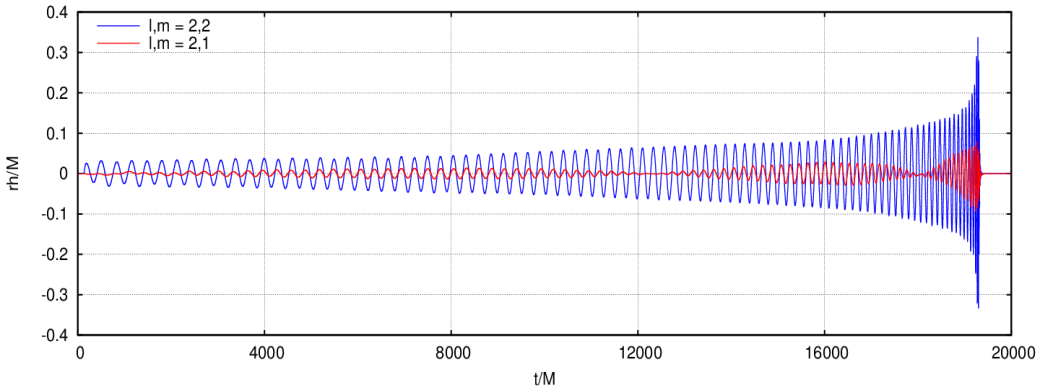

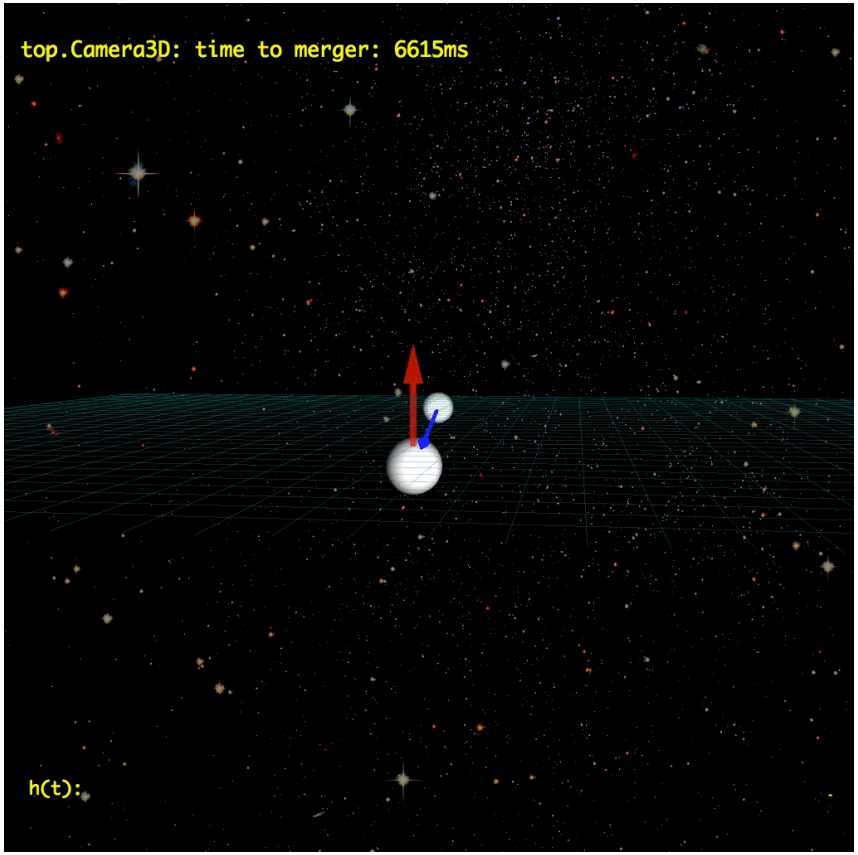

But we got about a million years late to measure it.

5. Numerical Relativity Waveform Catalogs

RIT BBH Waveform Catalog

- 3rd release of the BBH public RIT catalog at http://ccrg.rit.edu/~RITCatalog.html
- 777 waveforms: 477 nonprecessing + 300 precessing. $1/5 \leq q \leq 1$, $\frac{S}{m^2} \leq 0.95$, $\ell \leq 4$

Precesssing Cases:

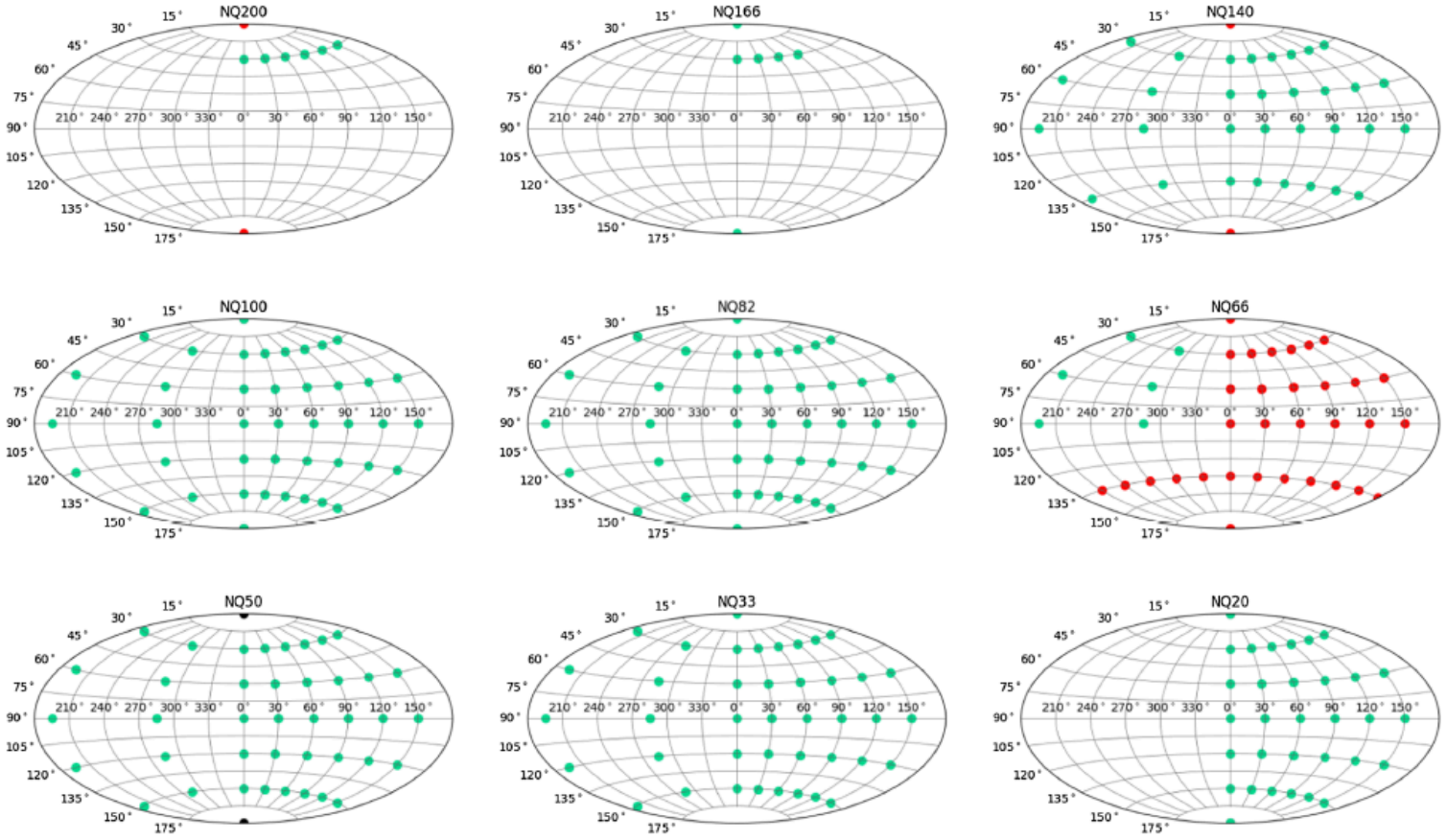

From: Healy and Lousto, Phys.Rev.D 102 (2020), 104018

FIG. 8. Initial parameters in the (q, θ_2, ϕ_2) space for the precessing binaries. Note that $(\chi_2 = 0.8, \theta_2, \phi_2)$ denotes the component of the dimensionless spin of the BH $i = 2$ from the direction of the orbital angular momentum. Each panel corresponds to a given mass ratio that covers the comparable masses binary range $q = 1, 0.82, 2/3, 1/3, 1/5$, and $q = 2, 5/3, 1.4$, where $q > 1$ means it is the smaller hole that is spinning. The dots in black denote the simulations of the catalog first release, the dots in red are those of the second release, and the dots in green are those of this third release.

GW150914: Heat Maps

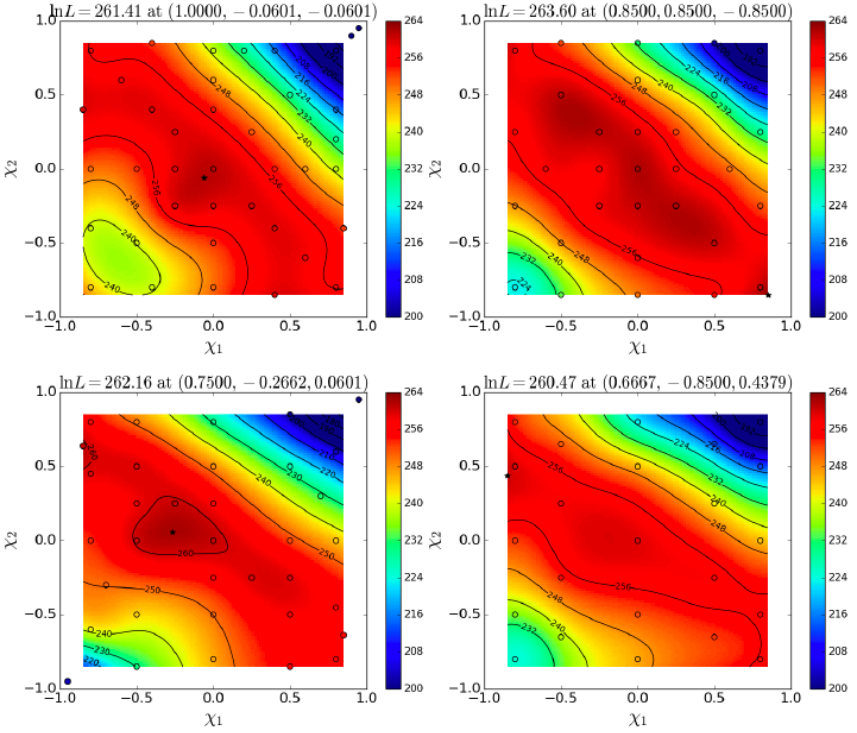

$$\ln \mathcal{L}(\boldsymbol{\lambda};\theta) = -\frac{1}{2}\sum_k \langle h_k(\boldsymbol{\lambda},\theta) - d_k | h_k(\boldsymbol{\lambda},\theta) - d_k\rangle_k - \langle d_k | d_k\rangle_k, \quad (1)$$

where h_k are the predicted response of the kth detector due to a source with parameters ($\boldsymbol{\lambda}$, θ) and d_k are the detector data in each instrument k; $\boldsymbol{\lambda}$ denotes the combination of redshifted mass M_z and the remaining intrinsic parameters (mass ratio and spins; with eccentricity ≈ 0) needed to uniquely specify the binary's dynamics; θ represents the seven extrinsic parameters (4 spacetime coordinates for the coalescence event and 3 Euler angles for the binary's orientation relative to the Earth); and $\langle a|b\rangle_k \equiv \int_{-\infty}^{\infty} 2df \tilde{a}(f)^* \tilde{b}(f)/S_{h,k}(|f|)$ is an inner product implied by the kth detector's noise power spectrum $S_{h,k}(f)$. In practice we adopt a low-frequency cutoff f_{min} so all inner products are modified to

$$\langle a|b\rangle_k \equiv 2\int_{|f|>f_{min}} df \frac{[\tilde{a}(f)]^* \tilde{b}(f)}{S_{h,k}(|f|)}. \quad (2)$$

The 90% confidence level gives

$$\begin{aligned} 0.570 < q &< 1.00, \\ 0.00 < |\chi_1| &< 1.00, \\ 0.00 < |\chi_2| &< 0.78, \\ -0.44 < \chi_{\rm eff} &< 0.14, \\ -0.44 < S_{hu} &< 0.14, \\ 66.3 < M_{total} &< 79.2 \end{aligned}$$

Compare these values to the GW150914 properties

$$\begin{aligned} 0.62 < q &< 0.99, \\ 0.04 < |\chi_1| &< 0.90, \\ 0.03 < |\chi_2| &< 0.78, \\ -0.29 < \chi_{\rm eff} &< 0.1, \\ 66.1 < M_{total} &< 75.2 \end{aligned}$$

Where M_{total} is given in solar mass $M_\odot$ units.

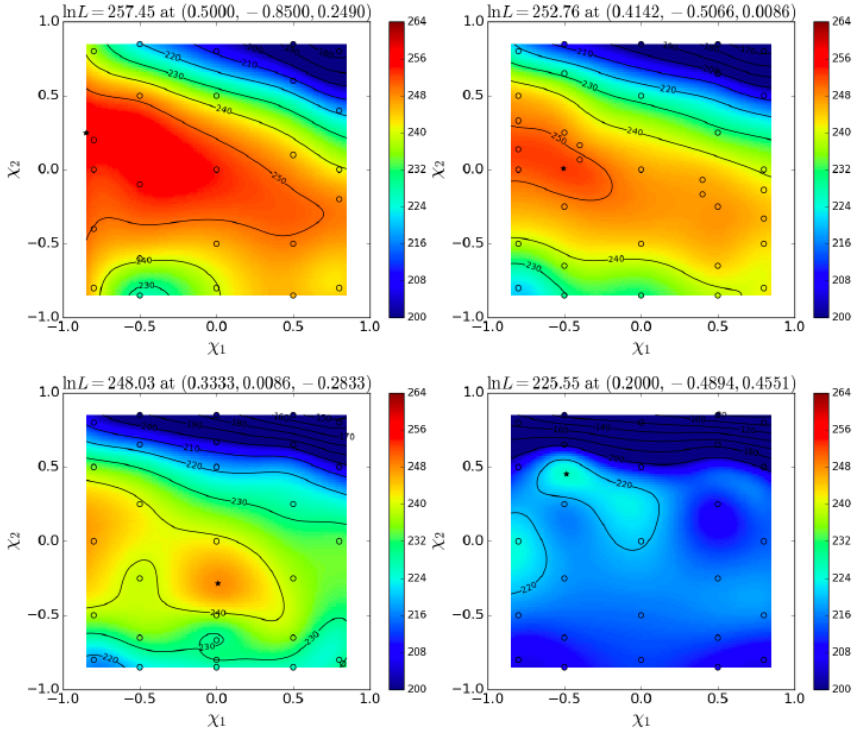

FIG. 4. Heat maps of the GW150914 likelihood for each of the eight mass ratio panels covering form $q = 1$ to $q = 1/5$ and aligned/antialigned individual spins. The individual panel with $q = 0.85$ contains the highest likelihood. Contour lines are in increments of 5. The interpolated $\ln \mathcal{L}$ maximum at its location in (q, χ_1, χ_2) space is given in each panel's title and denoted by the * in the plots.

Effective Spin variables*

Fig. 6 displays a comparative analysis of the single spin approximations to aligned binaries using a linear interpolation. The upper panel presents our preferred variables for the spin, S_{hu}

$$m^2\, S_{hu} = \left((1 + \frac{1}{2q})\, \vec{S}_1 + (1 + \frac{1}{2} q)\, \vec{S}_2 \right) \cdot \hat{L}, \qquad (3)$$

to describe the leading effect of hangup on the waveforms [30]. The lower panel displays a comparative heatmap using the common approximate model variable [97]

$$m^2\, \chi_{eff} = \left((1 + \frac{1}{q})\, \vec{S}_1 + (1 + q)\, \vec{S}_2 \right) \cdot \hat{L}.$$

The latter exhibits some "pinch" points around some simulations suggesting a remaining degeneracy by using χ_{eff}. Such features are not seen using the (normalized) variable S_{hu}, which represents a better fitting to waveform phases as shown in [30], suggesting again that it is a better (or at least a valid alternative) choice to describe aligned binaries.

[30] J. Healy and C. O. Lousto, Phys. Rev. **D97**, 084002 (2018), arXiv:1801.08162 [gr-qc].

S_{hu} perhaps a better spin variable for waveform modeling

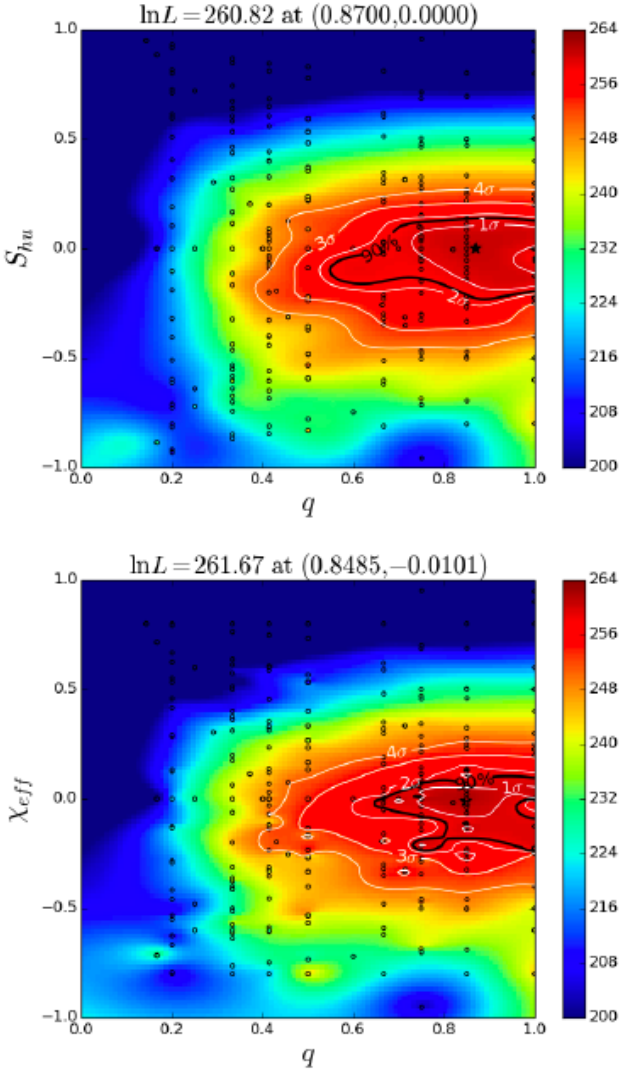

FIG. 6. Heat maps of the GW150914 likelihood for the aligned binary with effective variables S_{hu} and χ_{eff} versus mass ratios using linear interpolation. In black the 90% confidence contours and the interpolated $\ln \mathcal{L}$ maximum is given in each panel's title and denoted by the * in the plots.

GW150914: Precession

- Nearly 200 simulations
- One hole spinning,
- All orientations
  (q>1 is the smaller one)
- $\frac{s}{m^2} = 0.8$

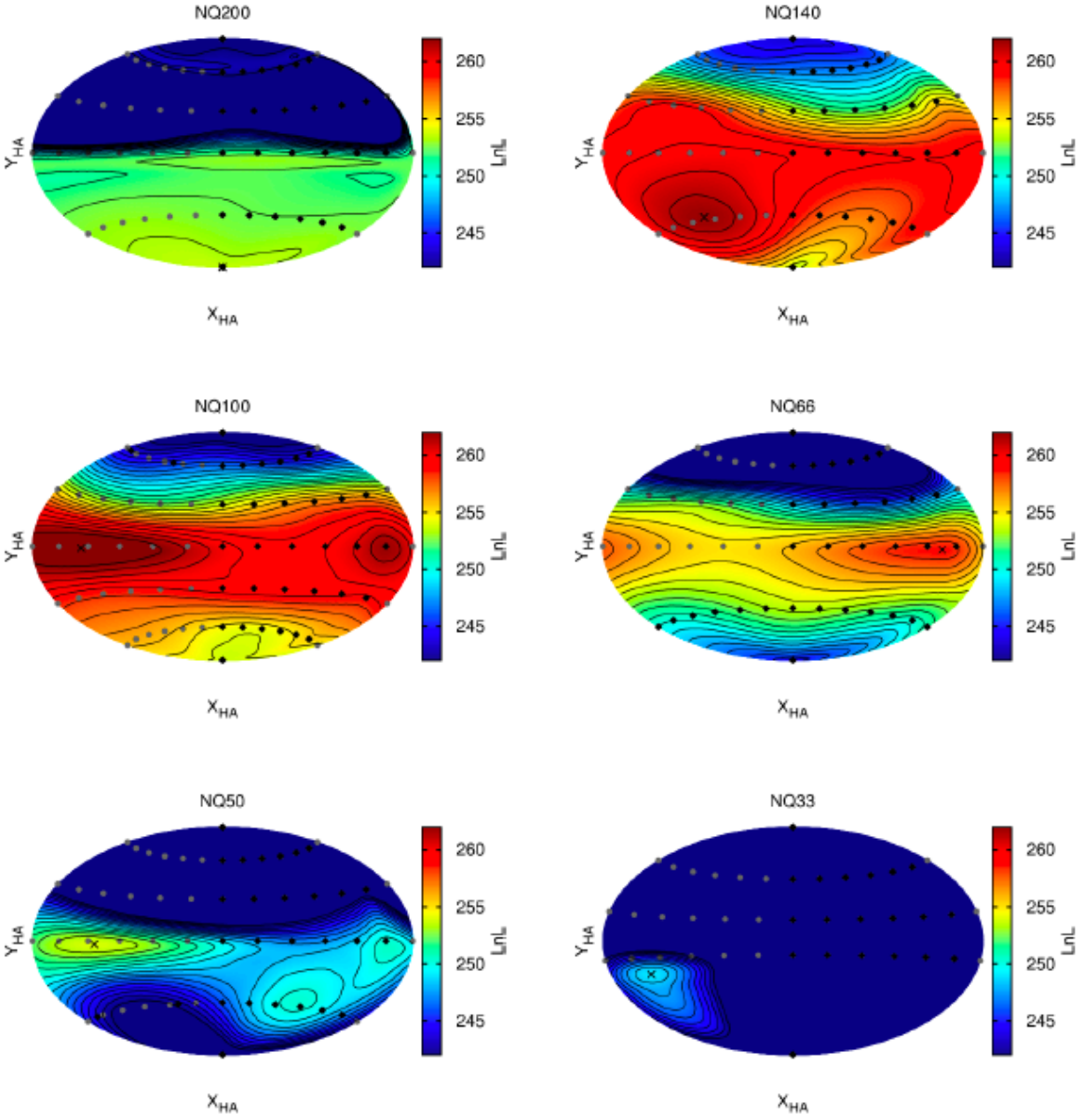

FIG. 8. Heat maps of the GW150914 likelihood for each of the six mass ratio panels covering form $q = 2$ to $q = 1/3$ (labeled from NQ200 to NQ33 respectively) and large black hole spin oriented over the sphere (interpolated using multiquadric radial basis functions between simulations). The individual panel with $q = 1$ contains the highest likelihood (near the orbital plane orientation), and it is bracketed by the $q = 1.4$ and $q = 0.66$ panels ($q > 1$ here means the smaller black hole is the one spinning). We have used Hammer-Aitoff coordinates X_{HA}, Y_{HA}, to represent the map and level curves. The interpolated $\ln \mathcal{L}$ maximum location is denoted by the an x in the plots, the black points are simulations, and the gray points are extrapolated simulations using the sinusoidal dependence of the azimuthal angle.

GW150914: Animation of Non Precessing and Precessing analysis* (2nd RIT Catalog)

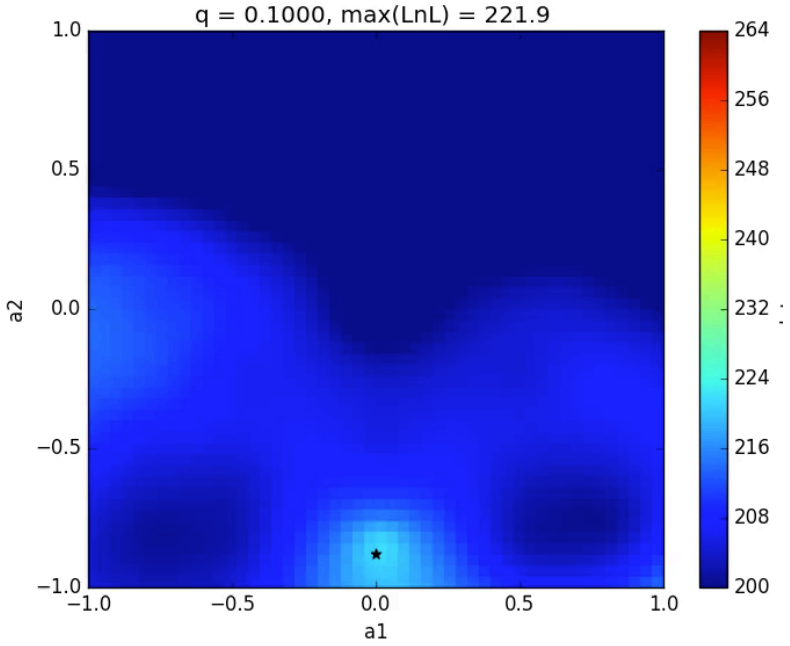

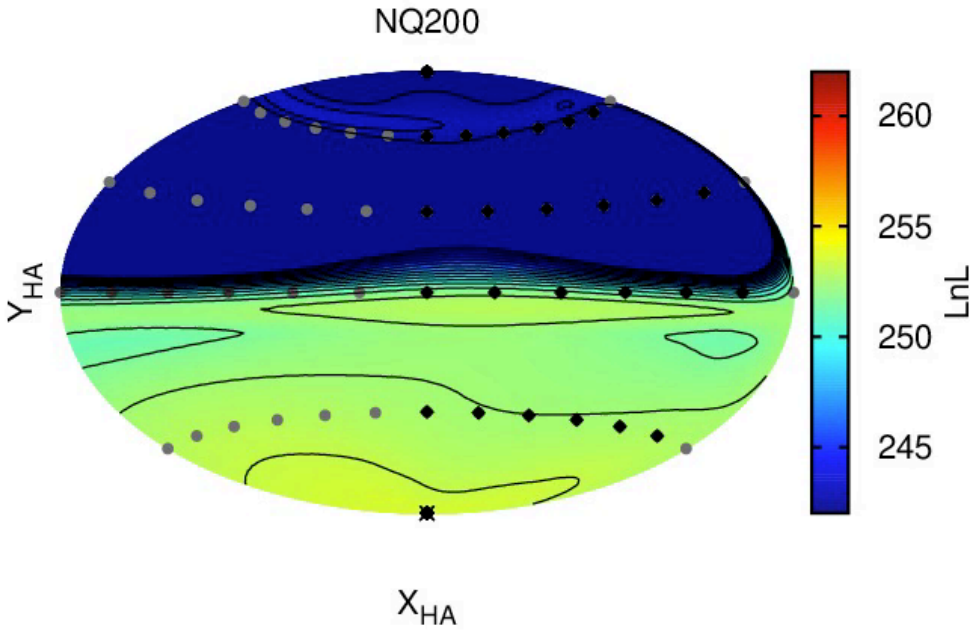

GW150914: Remnant properties

we find

$$0.039 < E_{rad}/m < 0.053$$
$$0.578 < \chi_f < 0.753$$
$$0 < V_{recoil} < 492[\mathrm{km/s}]$$

Comparing these ranges to the GW150914 properties paper [4] (and converting from total mass and final mass to energy radiated and propagating the errors appropriately)

$$0.041 < E_{rad}/m < 0.049$$
$$0.60 < \chi_f < 0.72$$

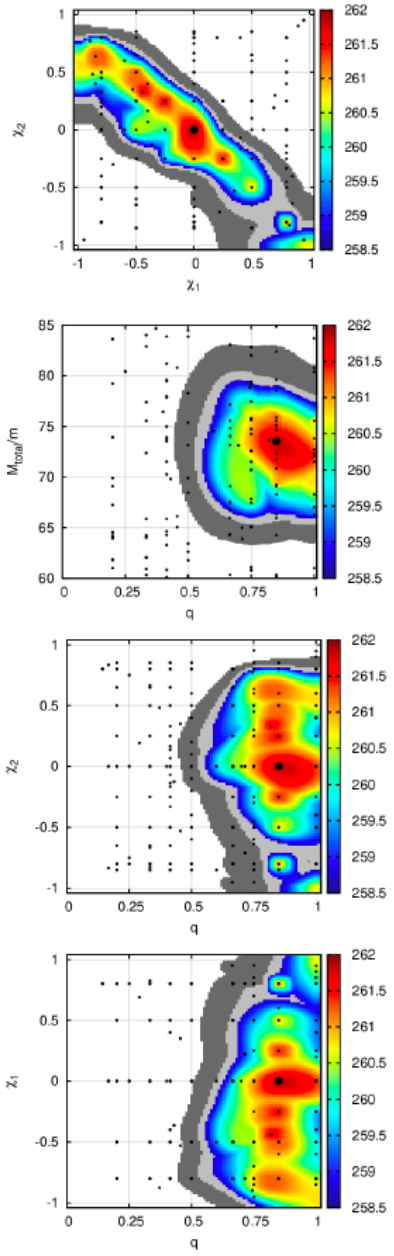

FIG. 5. 90% confidence interval heat maps of the GW150914 likelihood for the aligned binary mass ratio and individual spin parameters. The dark grey region constitutes the 99.7% (3σ) confidence interval range, and the light grey is the 95% (2σ) range. The colored region shows the $\ln \mathcal{L}$ of the values within the 90% confidence interval. The black points indicate the placement of the numerical simulations.

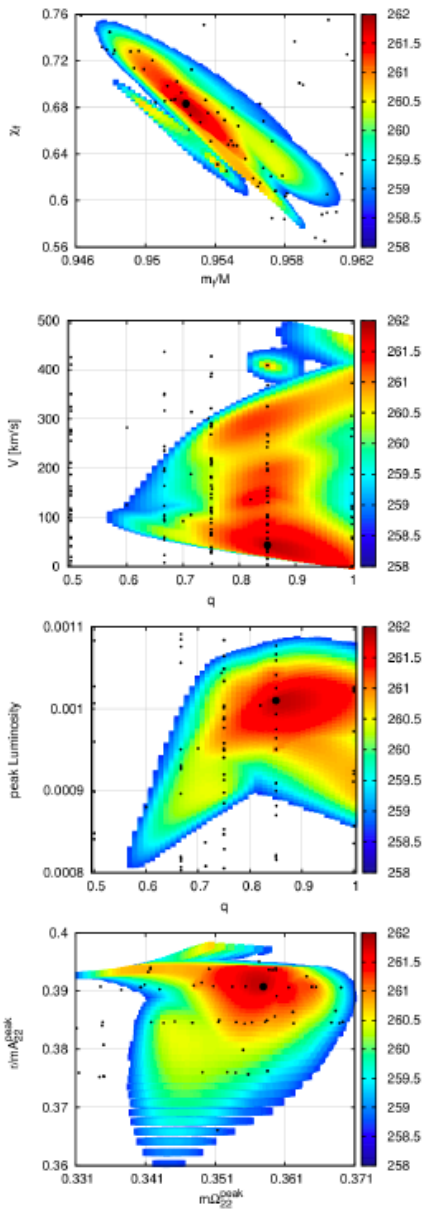

FIG. 7. Final parameter space heatmaps for simulations that fall within the 90% confidence interval for the final mass, spin, recoil, peak luminosity, and orbital frequency and strain amplitude at peak strain. A maximum $\ln \mathcal{L}$ is reached for $m_f/m = 0.952$, $\chi_f = 0.683$, $V = 44$ km/s, $L^{peak} = 1.01e-3$, $m\Omega_{22}^{peak} = 0.358$, and $(r/m)A_{22}^{peak} = 0.391$.

GW150914: Extrinsic parameters and waveforms

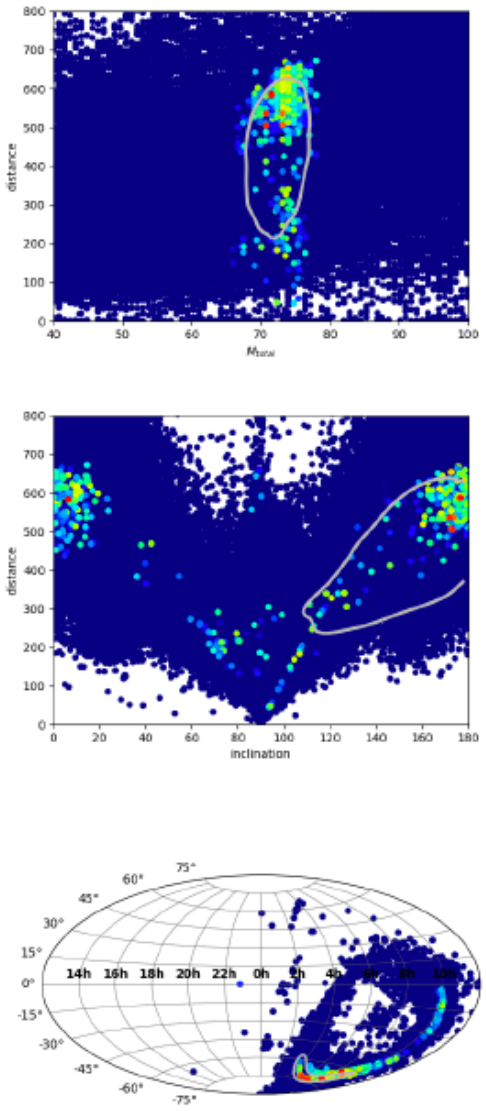

FIG. 9. We use the results of the Monte-Carlo intrinsic log-likelihood calculations (100 samples in M_{total} for each simulation in the catalog) to estimate the extrinsic parameters of GW150914. The gray boundary denotes the public LIGO GWTC-1 data and the colored points indicate simulations which fell within the $\ln \mathcal{L} > \max \ln \mathcal{L} - 3.125$, or roughly the 90% confidence interval. The dark blue background points denote simulations outside of the 90% confidence interval.

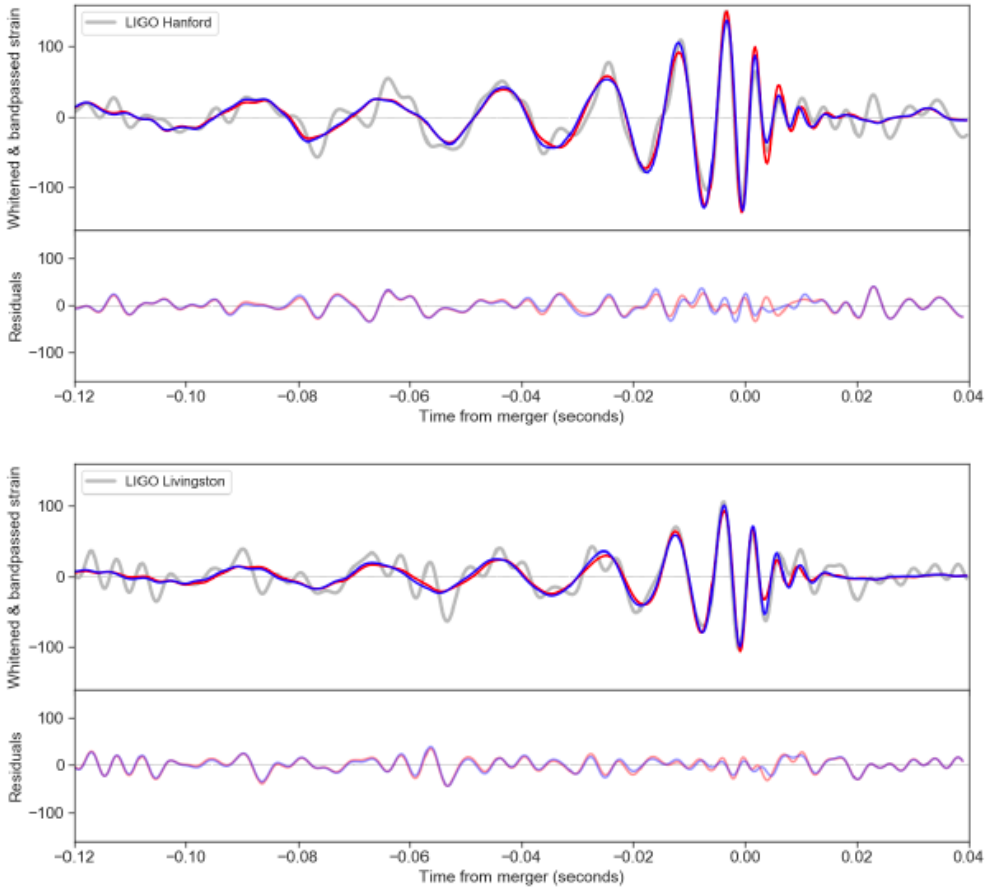

FIG. 10. Direct comparison of the highest $\ln \mathcal{L}$ nonprecessing simulation (RIT:BBH:0113 in red) and precessing simulation (RIT:BBH:0126 in blue) to the Hanford (top) and Livingston (bottom) GW150914 signals. The bottom panel in each figure shows the residual between the whitened NR waveform and detector signal.

TABLE I. Highest $\ln \mathcal{L}$ nonprecessing and precessing simulations. The nonprecessing simulation has highest overall $\ln \mathcal{L}$, and the precessing simulation has 13th highest.

Config.	q	$\vec{\chi}_1$	$\vec{\chi}_2$	$\vec{S}_{hu}/m^2$	$M_{total}/M_\odot$	$\ln \mathcal{L}$
RIT:BBH:0113	0.85	(0, 0, 0)	(0, 0, 0)	(0, 0, 0)	73.6	261.8
RIT:BBH:0126	0.75	(-0.46, -0.48, -0.44)	(0.06, -0.38, 0.12)	(-0.15, -0.42, -0.11)	72.5	260.5

GW170104 (O2)

This approach had already proven very successful when applied to GW170104*.

(It required an homogeneous set of simulations since the differences in LnL are subtle).

*J. Healy et al., Phys. Rev. D97, 064027 (2018)

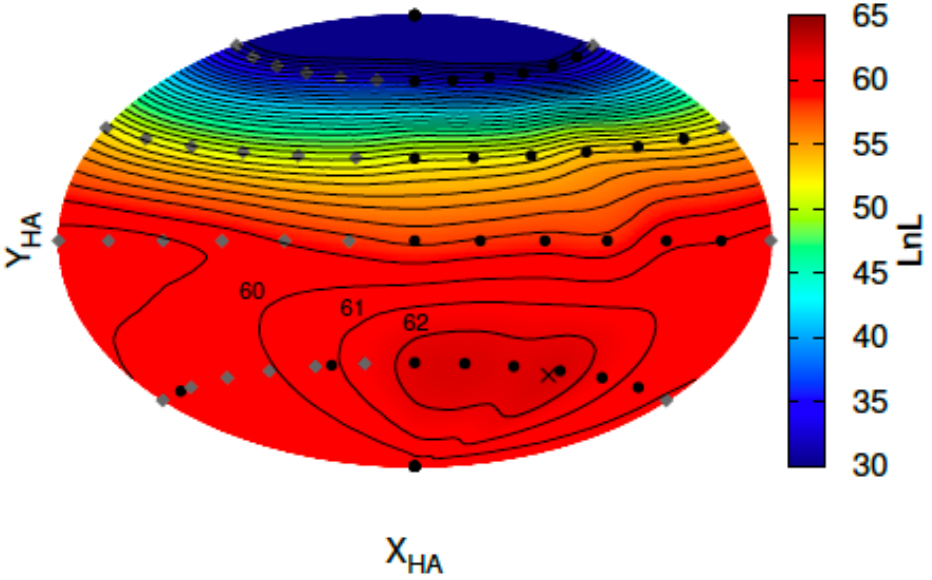

FIG. 8. The log-likelihood of the NQ50THPHI series [101] as a color map with red giving the highest $\ln \mathcal{L}$ and blue the lowest. The black dots (and grey diamonds, obtained by symmetry) represent the NR simulations and we have used Hammer-Aitoff coordinates X_{HA}, Y_{HA}, to represent the map and level curves with the top values of $\ln \mathcal{L} = 60, 61, 62$. The maximum, marked with an X, is located at TH=137, PH=87 reaching $\ln \mathcal{L} = 62.6$.

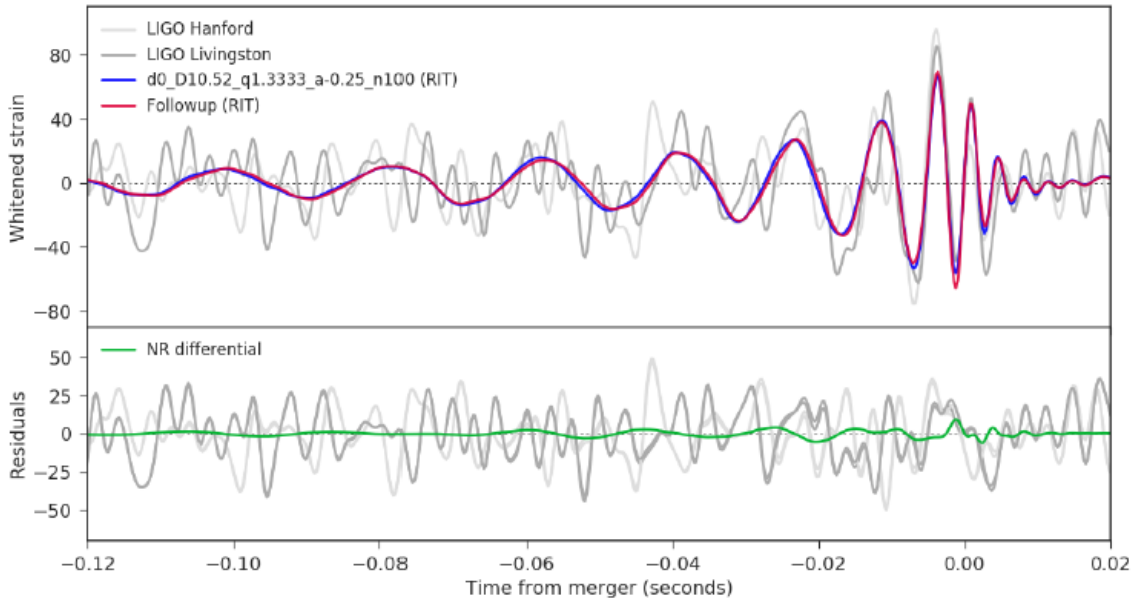

LIGO-Virgo O1/O2

PHYSICAL REVIEW D **102,** 124053 (2020)

We studied 13 BBH GW events of O1/O2 and found all intrinsic and extrinsic parameters

Application of the third RIT binary black hole simulations catalog to parameter estimation of gravitational-wave signals from the LIGO-Virgo O1 and O2 observational runs

James Healy, Carlos O. Lousto, Jacob Lange, and Richard O'Shaughnessy

Center for Computational Relativity and Gravitation, School of Mathematical Sciences, Rochester Institute of Technology, 85 Lomb Memorial Drive, Rochester, New York 14623, USA

(Received 30 September 2020; accepted 24 November 2020; published 22 December 2020)

Using exclusively the 777 full numerical waveforms of the third binary black hole RIT catalog, we reanalyze the ten black hole merger signals reported in LIGO/Virgo's O1/O2 observation runs. We obtain binary parameters, extrinsic parameters, and the remnant properties of these gravitational waves events which are consistent with, but not identical to, previously presented results. We have also analyzed three additional events (GW170121, GW170304, GW170727) reported by Venumadhav, Zackay, Roulet, Dai, and Zaldarriaga [Phys. Rev. D **101**, 083030 (2020)] and found closely matching parameters. We finally assess the accuracy of our waveforms with convergence studies applied to O1/O2 events and found them adequate for current estimation of parameters.

GW150914 (Revisited with 3rd RIT Catalog)

477 aligned spins BBH analysis

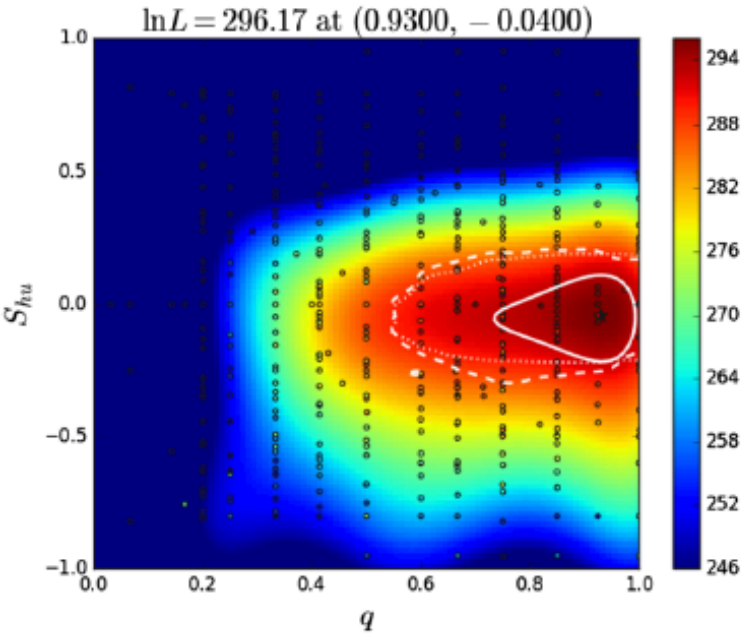

300 precessing simulations analysis

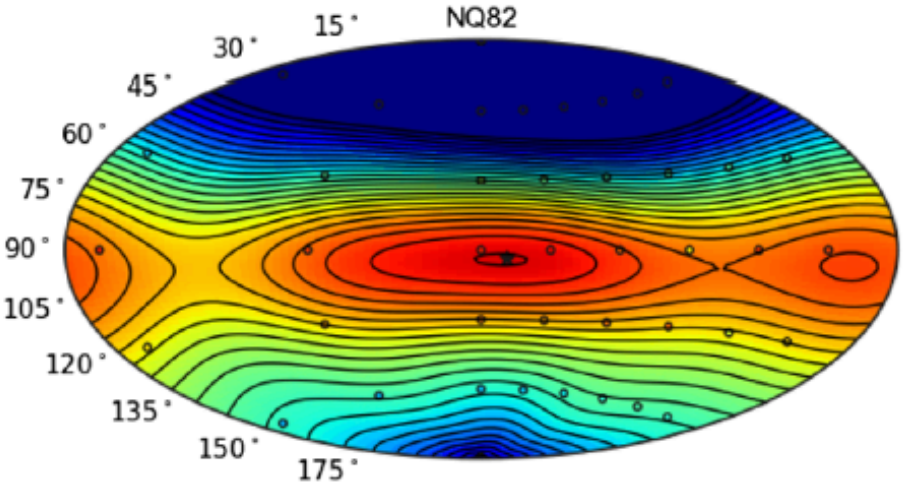

FIG. 3. Left panels: comparative analysis of the $S_{\rm hu}$ and $\chi_{\rm eff}$ spins versus q for GW150914 using the 477 nonprecessing binaries. The points show the parameters of these nonprecessing simulations. As described in the text, the color scale is based on an interpolation between each simulation's maximum $\mathcal{L}$ [i.e., $\max_M \mathcal{L}(M, q, \chi_{1,z}, \chi_{2,z})$] over (only) the two parameter dimensions shown in this plot. As in Fig. 2, the contours are 90% credible intervals of a posterior based on our full four-dimensional interpolated likelihood (solid); a reanalysis of the same likelihood, using conventional priors consistent with GWTC-1 (dashed); and the LIGO GWTC-1 analysis itself (dotted). Top right panel: top likelihood panel for the binary spin orientation for GW150914 using the 300 precessing simulations. The star labels the most likely orientation of the spin (essentially along the orbital plane) and NQ82 label means a mass ratio $q = 0.82$.

6. GW190521 (O3a)

GW190521 as a Highly Eccentric Black Hole Merger

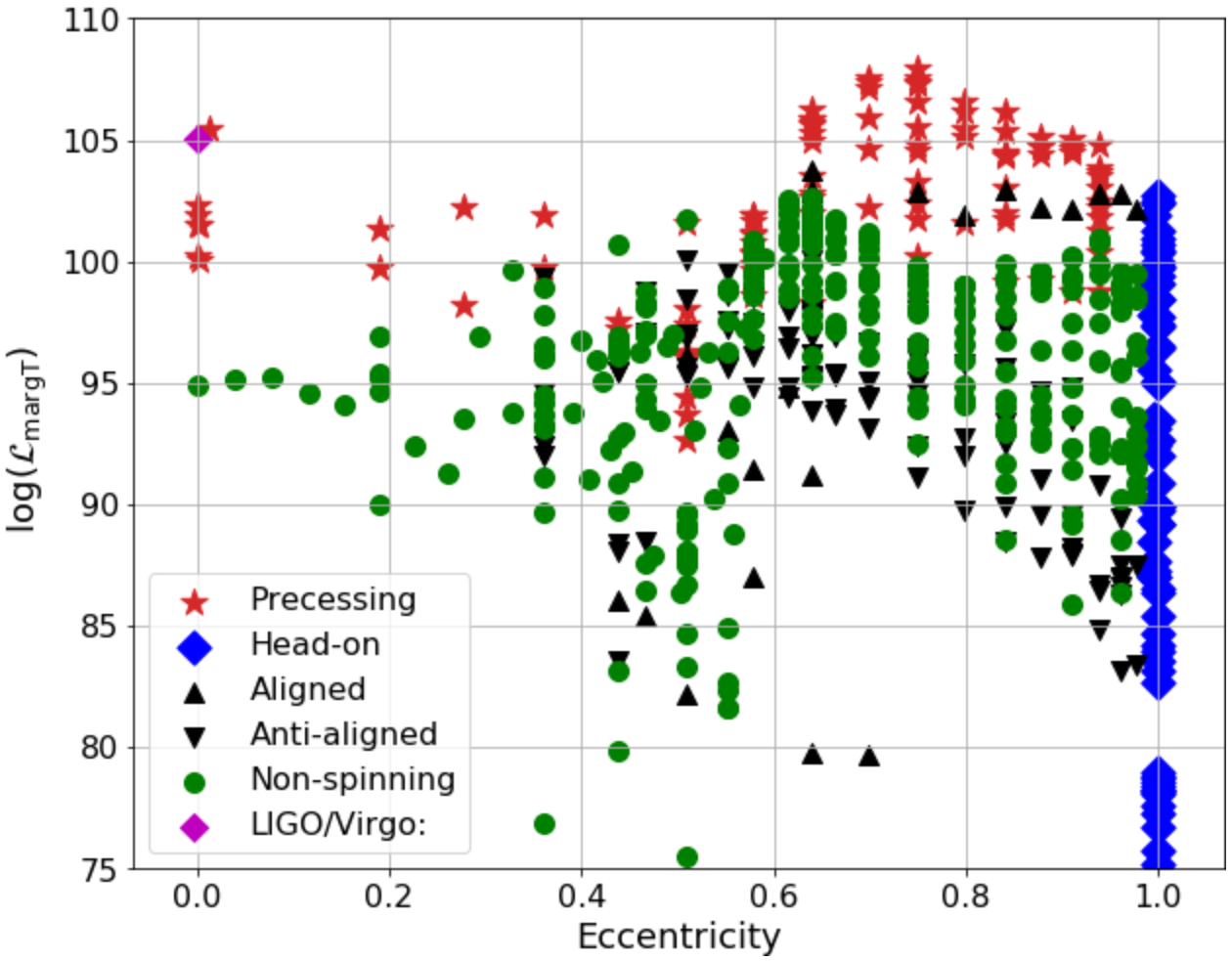

Marginalized likelihood as a function of eccentricity for our 600+ numerical relativity simulations

V. Gayathri et al. e-Print: 2009.05461 [astro-ph.HE]

Consistency of the cWB reconstruction of GW190521 with the numerical relativity simulations*

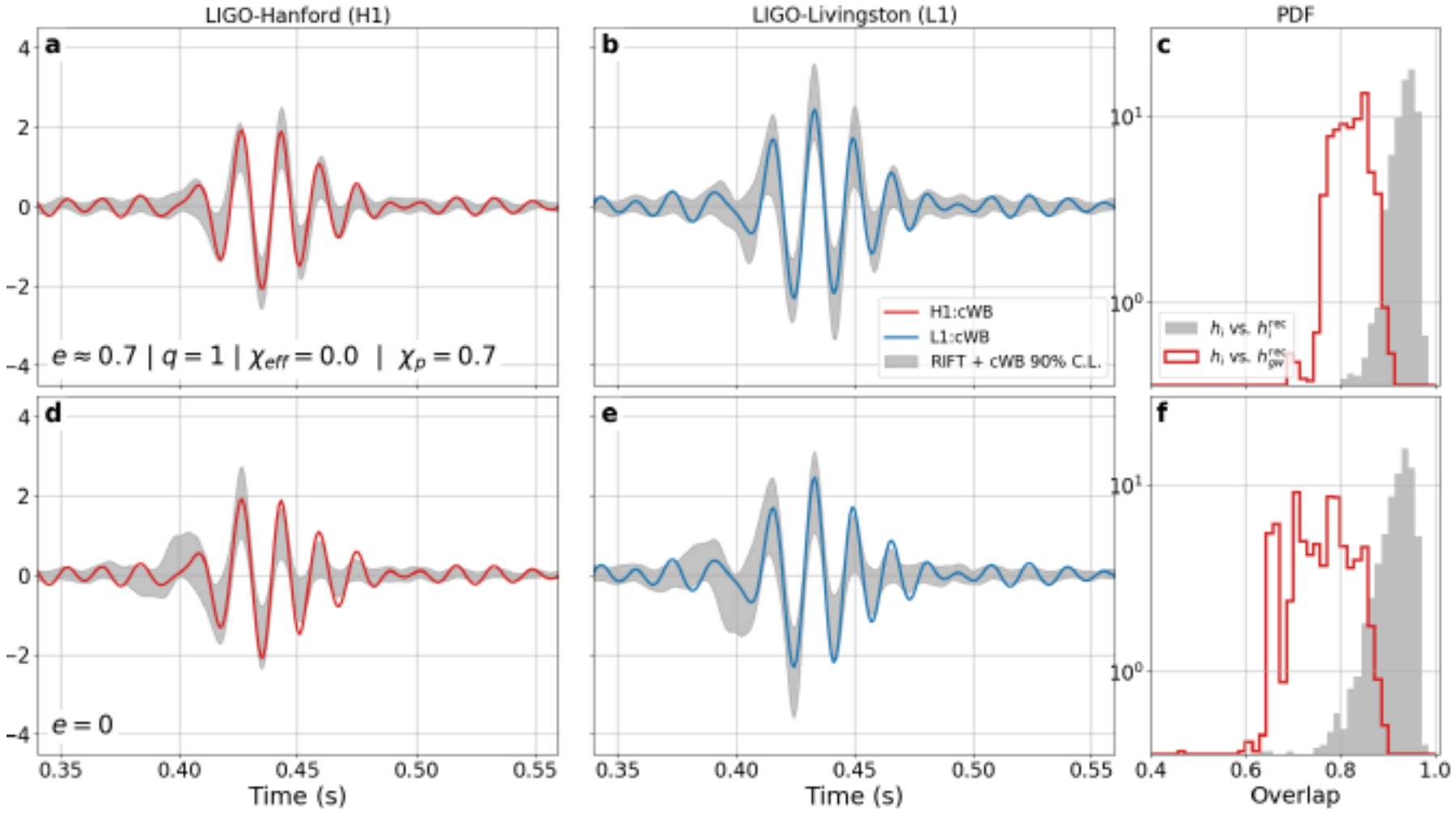

Hubble Constant Measurement with GW190521 as an Eccentric Black Hole Merger

V. Gayathri,[1] J. Healy,[2] J. Lange,[2] B. O'Brien,[1] M. Szczepanczyk,[1] I. Bartos,[1,*] M. Campanelli,[2] S. Klimenko,[1] C. Lousto,[2] and R. O'Shaughnessy[2,†]

[1] *Department of Physics, University of Florida, PO Box 118440, Gainesville, FL 32611-8440, USA*

[2] *Center for Computational Relativity and Gravitation, Rochester Institute of Technology, Rochester, NY 14623, USA*

ABSTRACT

Gravitational wave observations can be used to accurately measure the Hubble constant H_0 and could help understand the present discrepancy between constraints from Type Ia supernovae and the cosmic microwave background. Neutron star mergers are primarily used for this purpose as their electromagnetic emission can be used to greatly reduce measurement uncertainties. Here we estimate H_0 using the recently observed black hole merger GW190521 and its candidate electromagnetic counterpart found by ZTF using a highly eccentric explanation of the properties of GW190521. We find that the reconstructed distance of GW190521 and the redshift of the candidate host galaxy are more consistent with standard cosmology for our eccentric model than if we reconstruct the source parameters assuming no eccentricity. We obtain $H_0 = 88.6^{+17.1}_{-34.3}\,\mathrm{km\,s^{-1}Mpc^{-1}}$ for GW190521, and $H_0 = 73.4^{+6.9}_{-10.7}\,\mathrm{km\,s^{-1}Mpc^{-1}}$ in combination with the results of the neutron star merger GW170817. Our results indicate that future H_0 computations using black hole mergers will need to account for possible eccentricity. For extreme cases, the orbital velocity of binaries in AGN disks can represent a significant systematic uncertainty.

V. Gayathri et al. e-Print: 2009.14247 [astro-ph.HE]

H_0 Measurement with GW190521 as an Eccentric Black Hole Merger

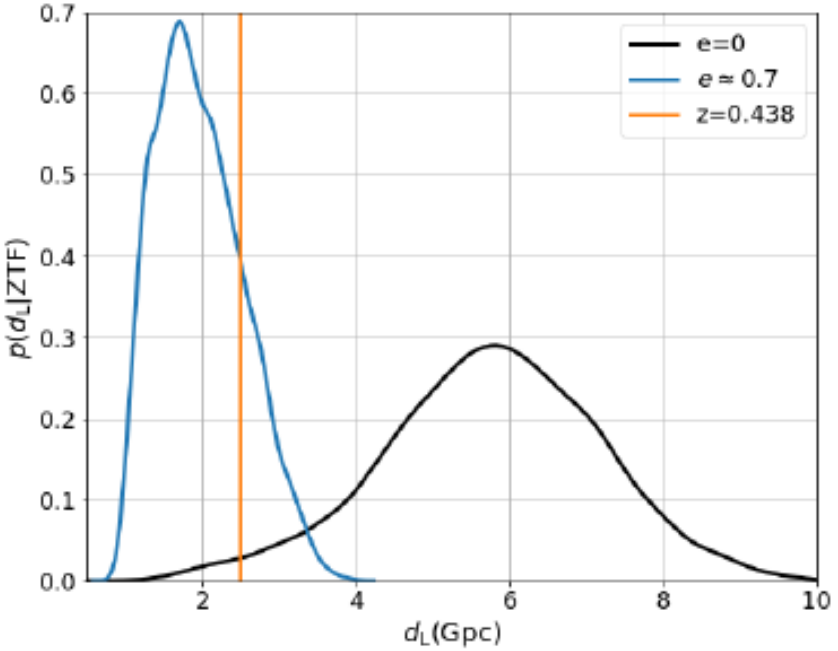

Figure 1. Luminosity distance probability distribution obtained using NRSur7dq4 gravitational waveforms (Varma et al. 2019) assuming eccentricity $e = 0$ (red), and using the UF/RIT model with eccentricity $e \approx 0.7$ (Gayathri et al. 2020b) (black). These distributions are obtained using RIFT algorithm for fixed source direction to that of the ZTF source. The vertical line shows the distance of the ZTF source assuming Planck 2018 cosmology (Aghanim et al. 2018).

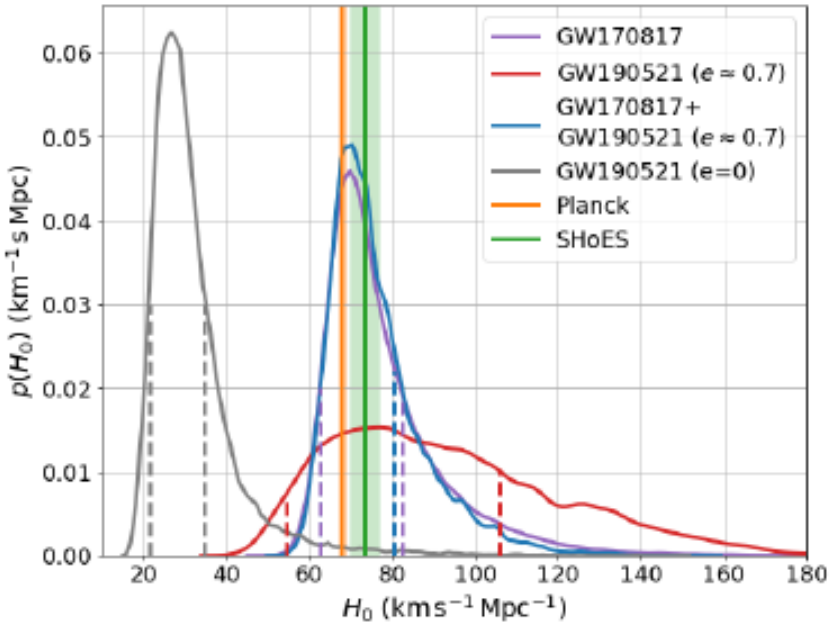

Figure 3. H_0 measurements for GW190521 with its ZTF candidate counterpart and GW170817. The following H_0 probability densities are shown: GW170817 (purple); GW190521 with eccentric model (red); combined GW170817 and GW190521 with eccentric model (blue); GW190521 with $e = 0$ (gray); cosmic microwave background results by Planck (orange); and type Ia supernova results by ShoES (green). Shaded areas for the latter two results show 95% confidence intervals. Vertical dashed lines for the gravitational-wave results indicate 68% credible intervals.

7. Discussion

Discussion

- ✓ We have developed a complete and independent method to analyze GW signals from BBH with NR solutions to GR (Without resourcing to phenomenology)
- ✓ Applied to O1/O2, and to O3+:
- ○ Interesting sources to detect yet
  - ➢ Highly eccentric BBHs?
  - ➢ Very highly spinning BHs (s > 0.9)
  - ➢ Not comparable BBH mass ratios (q < 1/5-1/10)
  - ➢ BH-NS systems (q ~ 1/7– 1/20)
- ❖ RIT Catalog3: Complete single spinning q's; Complete aligned spins 0.95; down to q -> 1/15.
- ❖ RIT Catalog4: Will include 600+ eccentric waveforms, reaching over 1500 simulations.
- ❖ A collection of NR catalogs (RIT+SXS+GT+BAM+) can be used for even better coverage.
- ❖ Improved coverage and accuracy for 3G detectors and for LISA.

8. Bonus

Exploring the small mass ratio binary black hole merger with Numerical Relativity

- First full numerical simulation 100:1 for two orbits before merger (Proof of principle):

C. O. Lousto and Y. Zlochower, Phys. Rev. Lett. **106**, 041101 (2011), arXiv:1009.0292 [gr-qc].

- More recently, we studied the GW beaconing with precessing q=1/7, q=1/15 binaries and found excellent results with updated techniques and AMR grid:

C. O. Lousto and J. Healy, Phys. Rev. **D99**, 064023 (2019), arXiv:1805.08127 [gr-qc].

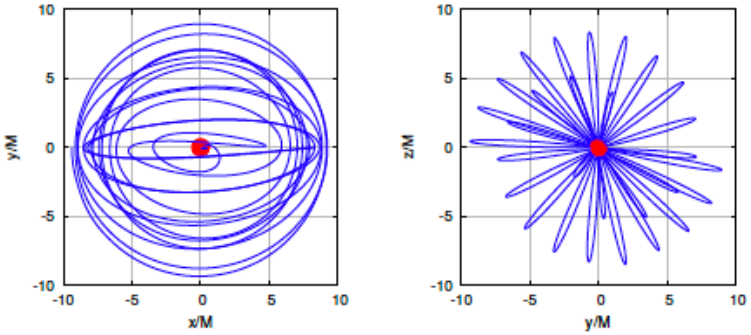

- We will revisited the scenario of the nonspinning small mass ratio binaries as we did for up to q=1/10 in: J. Healy, C. O. Lousto, and Y. Zlochower, Phys. Rev. **D96**, 024031 (2017), arXiv:1705.07034 [gr-qc].

-> But we now push it to q=1/15, 1/32, 1/64, and 1/128

Numerical Simulation

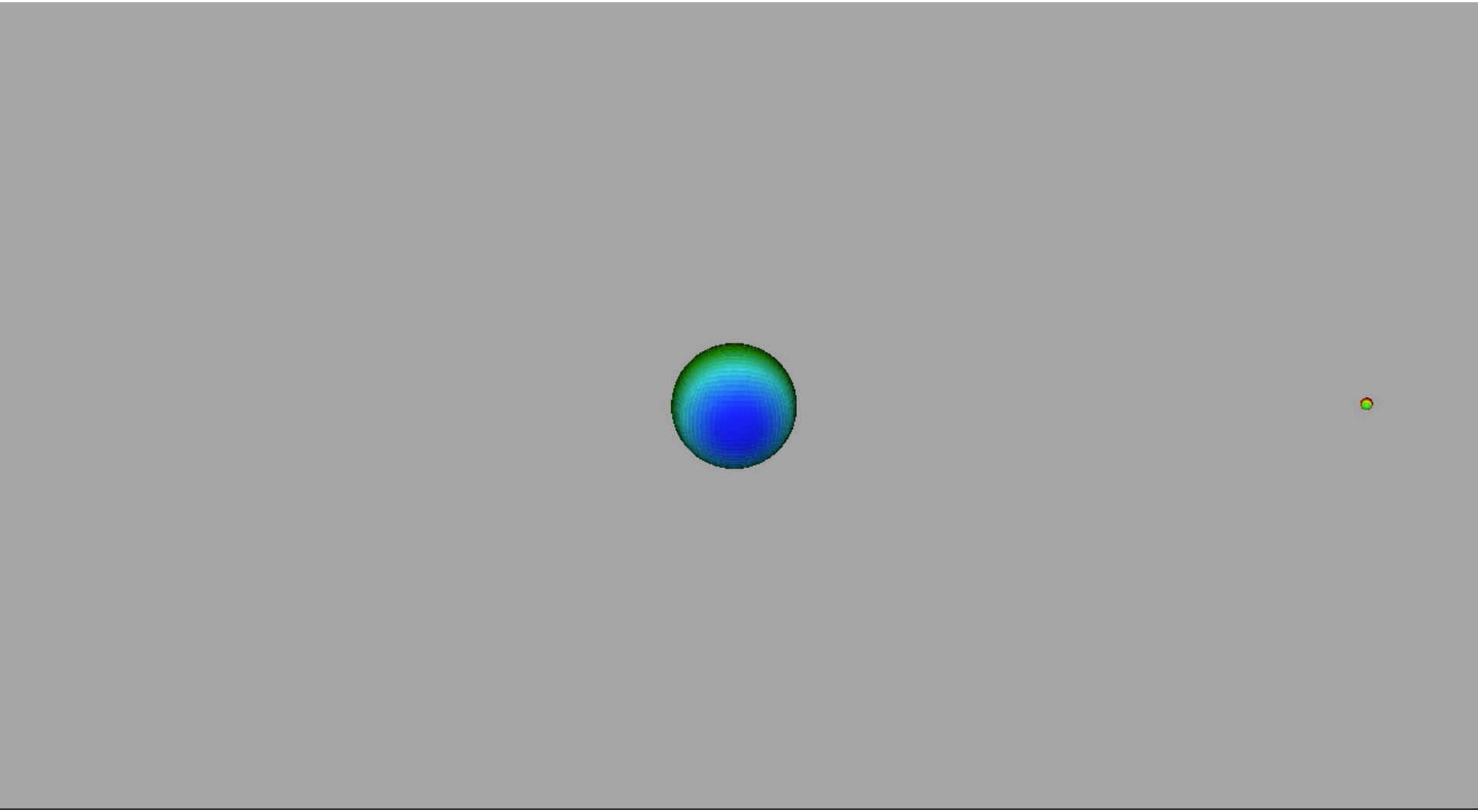

128:1 merger orbit and horizons curvature

Lousto & Healy, Phys.Rev.Lett. 125 (2020), 191102

Numerical Simulations

Consistency:

TABLE II. Final properties for the sequence of the $q = 1/15, 1/32, 1/64, 1/128$ simulations includes the final black hole mass $M_{\rm rem}/m$ and spin $\alpha_{\rm rem}$, the recoil velocity v_m, and the peak luminosity $\mathcal{L}_{\rm peak}$ and waveform frequency $\omega_{22}^{\rm peak}$ at the maximum amplitude $h_{\rm peak}$. Also given are the initial simple proper distance, SPD, number of orbits to merger N, and a consistency check of the differences between the final mass and spin, $\Delta M_{\rm rem}/m$, $\Delta\alpha_{\rm rem}$, calculated from the horizon and from the radiated energy and angular momentum.

q	$M_{\rm rem}/m$	$\Delta M_{\rm rem}/m$	$\alpha_{\rm rem}$	$\Delta\alpha_{\rm rem}$	v_m[km/s]	$\mathcal{L}_{\rm peak}[ergs/s]$	$m\omega_{22}^{\rm peak}$	$(r/m)h_{\rm peak}$	SPD/m	N
1/15	0.9949	9×10^{-5}	0.1891	2.3×10^{-4}	34.24	1.665e+55	0.2882	0.0849	10.13	10.01
1/32	0.9979	3×10^{-5}	0.1006	2.5×10^{-3}	9.14	4.260e+54	0.2820	0.0424	9.51	13.02
1/64	0.9990	5×10^{-7}	0.0520	2.8×10^{-4}	2.34	1.113e+54	0.2812	0.0220	8.22	9.98
1/128	0.9996	4×10^{-5}	0.0239	2.7×10^{-3}	0.96	3.313e+53	0.2746	0.0116	8.19	12.90

Speeds ~ q:
2.2M/h (q=1/15 with 8th order) on 8 nodes (448 cores) in Frontera (TACC).
1.1 M/h (q=1/32),
0.6M/h (q=1/64),
0.32M/h (q=1/128)

T_{merger} ~ (83.2M) $eta^{-0.56}$, $eta=m_1m_2/m^2$

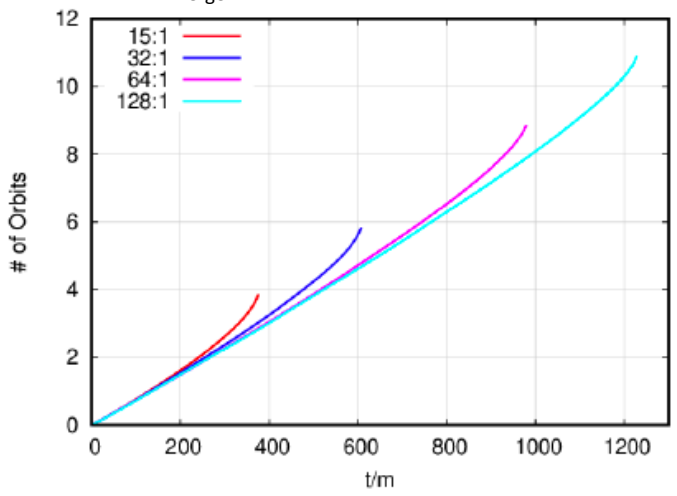

FIG. 2. Comparative number of orbits and time to merger, from a fiducial orbital frequency $m\Omega_i = 0.0465$ for the $q = 1/15, 1/32, 1/64, 1/128$ simulations.

Numerical Simulations

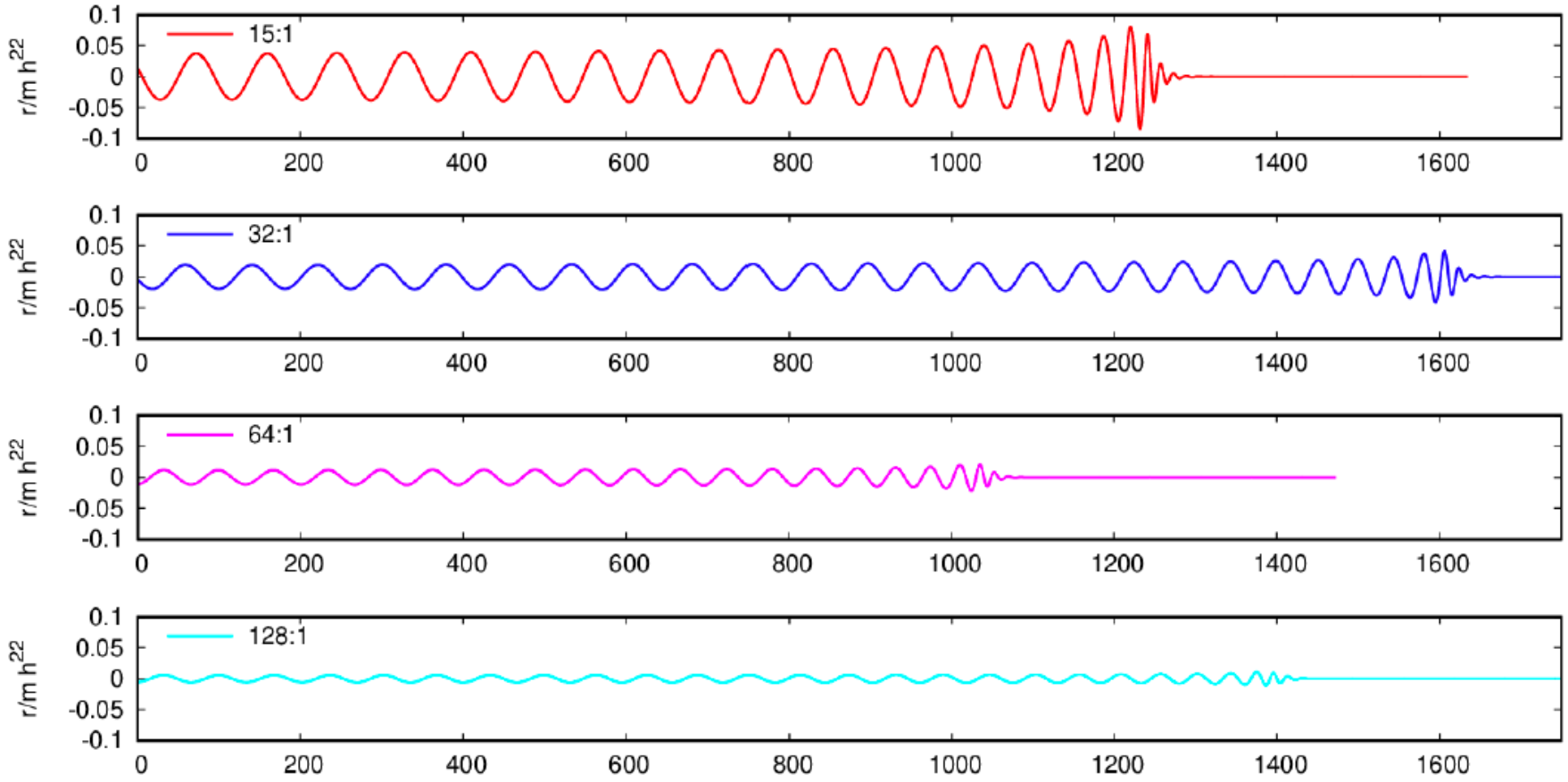

FIG. 2. (2,2) modes (real part) of the strain waveforms versus time (t/m), for the $q = 1/15, 1/32, 1/64, 1/128$ simulations.

Numerical Simulations*

Convergence:

TABLE I. The energy radiated, $E_{\rm rad}/m$, angular momentum radiated $J_{\rm rad}/m^2$, recoil velocity v_m, and the peak luminosity $\mathcal{L}_{\rm peak}$, waveform frequency $\omega_{22}^{\rm peak}$ at the maximum amplitude $h_{\rm peak}$, for each resolution of the $q = 1/15$ simulations, starting at SPD=$10m$. All quantities are calculated from the gravitational waveforms. Extrapolation to infinite resolution and order of convergence is derived.

resolution	$E_{\rm rad}/m$	$J_{\rm rad}/m^2$	v_m[km/s]	$\mathcal{L}_{\rm peak}$[ergs/s]	$m\omega_{22}^{\rm peak}$	$(r/m)h_{\rm peak}$
n084	0.002366	-0.029385	31.45	1.585e+55	0.2906	0.08471
n100	0.002418	-0.029945	33.54	1.649e+55	0.2863	0.08485
n120	0.002436	-0.030097	34.24	1.665e+55	0.2882	0.08489
n$\to\infty$	0.002444	-0.030148	34.56	1.670e+55	0.2897	0.08489
order	6.19	7.58	6.41	8.11	4.71	8.83

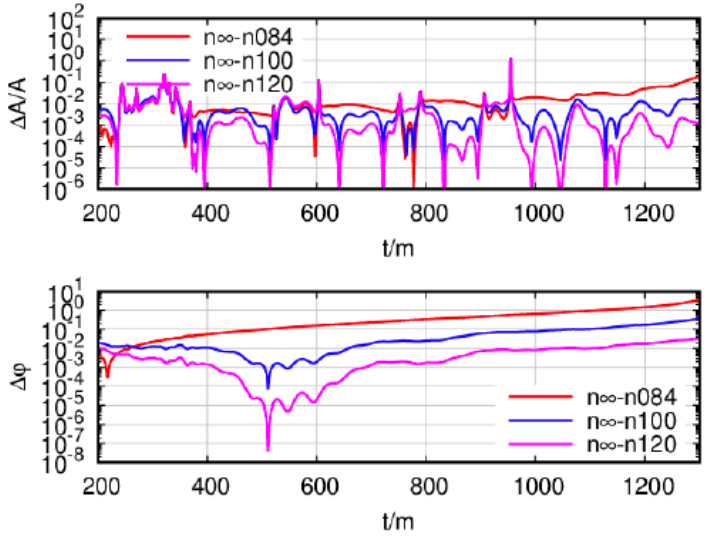

FIG. 1. Difference between each resolution of the $q = 1/15$ strain waveform with the calculated infinite resolution waveform for the amplitude and phase of the (2,2) mode.

Results

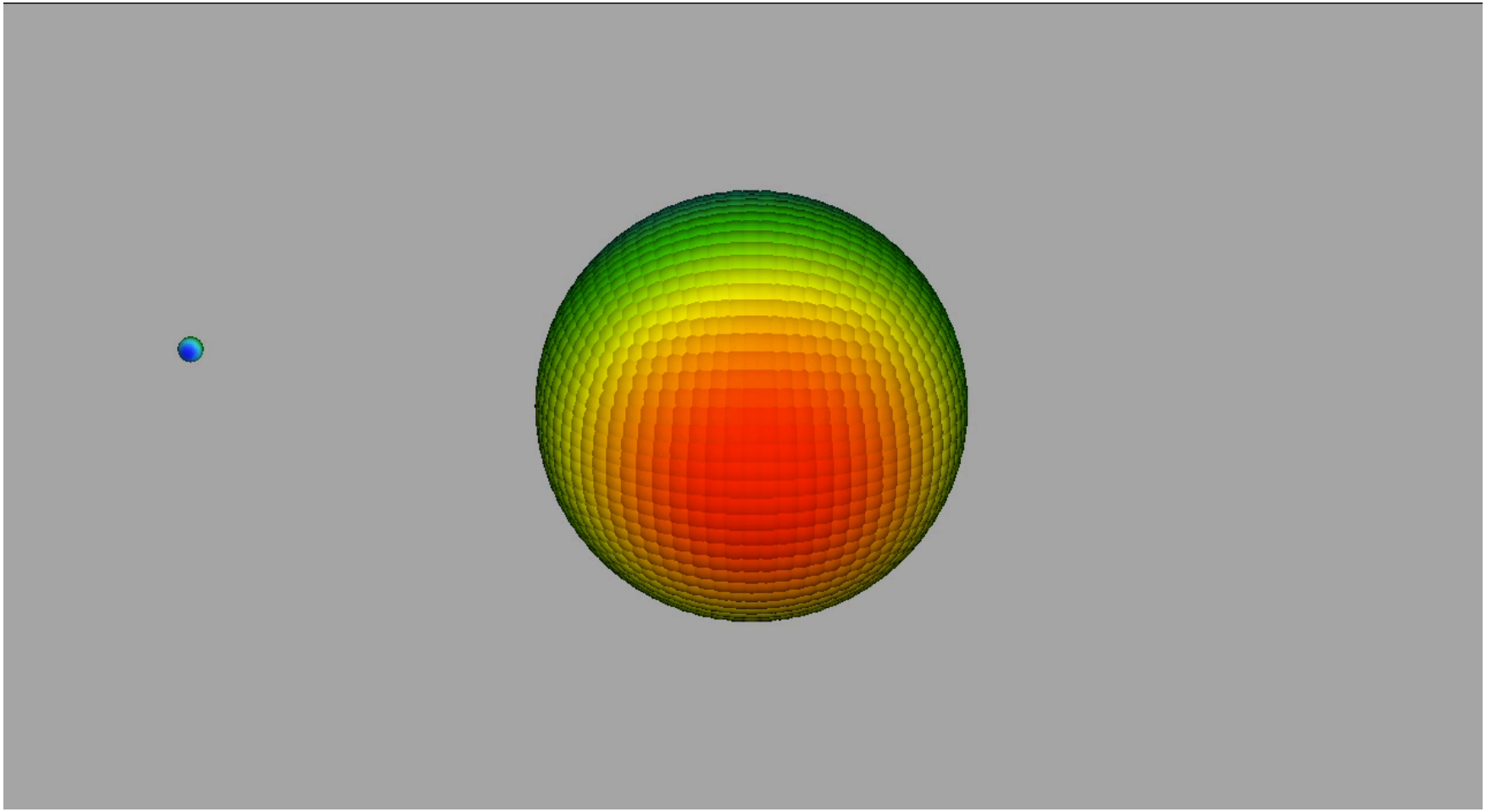

128:1 merger horizons (rescaled) Curvature K
Viz: Nicole Rosato.

Analysis

$$\frac{M_{\rm rem}}{m} = (4\eta)^2 \left\{ M_0 + K_{2d}\,\delta m^2 + K_{4f}\,\delta m^4 \right\} + \left[1 + \eta(\tilde{E}_{\rm ISCO} + 11) \right] \delta m^6, \qquad (1)$$

where $\delta m = (m_1 - m_2)/m$ and $m = (m_1 + m_2)$ and $4\eta = 1 - \delta m^2$.

$$\alpha_{\rm rem} = \frac{S_{\rm rem}}{M_{\rm rem}^2} = (4\eta)^2 \left\{ L_0 + L_{2d}\,\delta m^2 + L_{4f}\,\delta m^4 \right\} + \eta \tilde{J}_{\rm ISCO} \delta m^6. \qquad (2)$$

$$v_m = \eta^2 \delta m \left(A + B\,\delta m^2 + C\,\delta m^4 \right). \qquad (3)$$

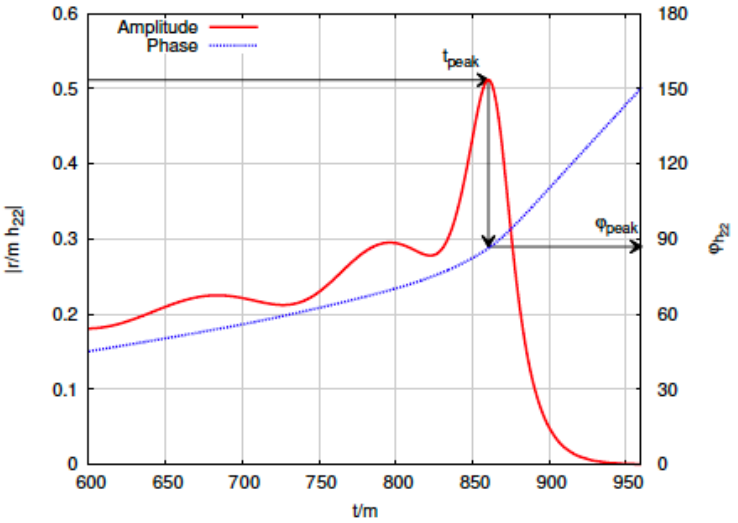

$$h_{\rm peak} = (4\eta)^2 \left\{ H_0 + H_{2d}\,\delta m^2 + H_{4f}\,\delta m^4 \right\} + \eta\,\tilde{H}_p\,\delta m^6, \qquad (4)$$

where $\tilde{H}_p(\alpha_{\rm rem})$ is the particle limit, taking the value $H_p(0) = 1.4552857$ in the nonspinning limit [18].

$$\mathcal{L}_{\rm peak} = (4\eta)^2 \left\{ N_0 + N_{2d}\,\delta m^2 + N_{4f}\,\delta m^4 \right\}. \qquad (5)$$

$$m\omega_{22}^{\rm peak} = (4\eta) \left\{ W_0 + W_{2d}\,\delta m^2 + W_{4f}\,\delta m^4 \right\} + \tilde{\Omega}_p\,\delta m^6, \qquad (6)$$

where $\tilde{\Omega}_p(\alpha_{\rm rem})$ is the particle limit, taking the value $\tilde{\Omega}_p(0) = 0.279525$ in the nonspinning limit [18].

[18] A. Bohé *et al.*, Phys. Rev. **D95**, 044028 (2017), arXiv:1611.03703 [gr-qc].

Analysis

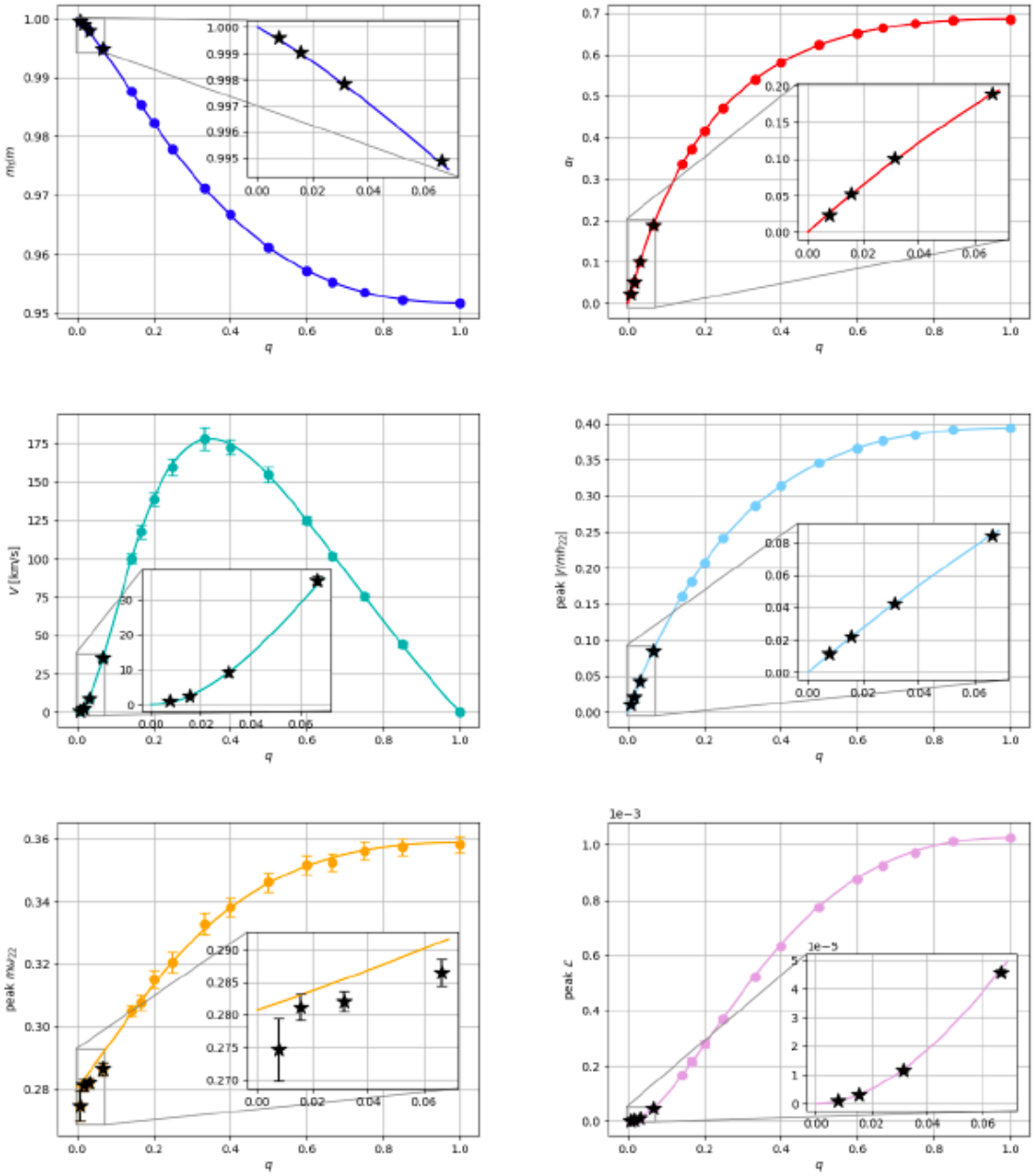

TABLE III. Fitting coefficients of the phenomenological formulas (1)-(6)

M_0	K_{2d}	K_{4f}
0.95165 ± 0.00002	1.99604 ± 0.00029	2.97993 ± 0.00066
L_0	L_{2d}	L_{4f}
0.68692 ± 0.00065	0.79638 ± 0.01086	0.96823 ± 0.02473
A	B	C
-8803.17 ± 104.60	-5045.58 ± 816.10	1752.17 ± 1329.00
$N_0 \times 10^3$	$N_{2d} \times 10^4$	$N_{4f} \times 10^4$
(1.0213 ± 0.0004)	(-4.1368 ± 0.0652)	(2.46408 ± 0.1485)
W_0	W_{2d}	W_{4f}
0.35737 ± 0.00097	0.26529 ± 0.01096	0.22752 ± 0.01914
H_0	H_{2d}	H_{4f}
0.39357 ± 0.00015	0.34439 ± 0.00256	0.33782 ± 0.00584

[13] J. Healy, C. O. Lousto, and Y. Zlochower, Phys. Rev. **D96**, 024031 (2017), arXiv:1705.07034 [gr-qc].

FIG. 3. Final mass, spin, recoil velocity, peak amplitude, frequency, and luminosity. Predicted vs. current results for the $q = 1/15, 1/32, 1/64, 1/128$ simulations. Each panel contains the prediction from the original fits in Ref. [13] (solid line), data used to determine the original fits (filled circles), and the data for the current results (stars). An inset in each panel zooms in on the new simulations. Again, we stress no fitting to the new data is performed in this plot.

Conclusions

- We have passed all first accuracy tests up to q=1/128:
  - ✓ Assessed errors ~2% from remnant and peak waveform
  - ✓ Convergence and horizon-radiation consistency
- Adding spin to large black hole with same grid is straightforward
- Can still use speed ups for massive productions for applications to
  - 3G GW detectors
  - LISA for calibration of perturbative techniques